Acoustics of bubbles trapped in microgrooves: From isolated subwavelength resonators to superhydrophobic metasurfaces

Ory Schnitzer,[1] Rodolfo Brandão,[1] and Ehud Yariv[2]
[1]*Department of Mathematics, Imperial College London, London SW7 2AZ, United Kingdom*
[2]*Department of Mathematics, Technion — Israel Institute of Technology, Haifa 32000, Israel*

(Received 1 February 2019; revised manuscript received 21 March 2019; published 31 May 2019)

We study the acoustic response of flat-meniscus bubbles trapped in the grooves of a microstructured hydrophobic substrate immersed in water. In the first part of the paper, we consider a single bubble subjected to a normally incident plane wave. We use the method of matched asymptotic expansions, based on the smallness of the gas-to-liquid density ratio, to describe the near field of the groove, where the compressibility of the liquid can be neglected, and an acoustic region, on the scale of the wavelength, which is much larger than the groove opening in the resonance regime of interest. We find that bubbles trapped in grooves support multiple subwavelength resonances, which are damped—radiatively—even in the absence of dissipation. Beyond the fundamental resonance, at which the pinned meniscus is approximately parabolic, we find a sequence of higher-order antiresonance and resonance pairs; at the antiresonances (whose frequencies are independent of the gas properties and groove size), the gas is idle and the scattering vanishes, while the liquid pressure is in balance with capillary forces.

In the second part of the paper, we develop a multiple-scattering theory for dilute arrays of trapped bubbles, where the frequency response of a single bubble enters via a scattering coefficient. For an infinite array and subwavelength spacing between the bubbles, the resonances are suppressed by an interference effect associated with the strong logarithmic interactions between quasistatic line sources; the antiresonances are robust. In contrast, for finite arrays, however large, we find strong and highly oscillatory deviations from the frequency response of an infinite array in a sequence of intervals about the resonance frequencies of a single bubble; these deviations are shown to be associated with edge excitation, in the finite case, of surface "spoof plasmon" waves, which exist in the infinite case precisely in the said frequency intervals; the resonant peaks in these intervals correspond to the formation of standing surface waves in the finite array.

DOI: 10.1103/PhysRevB.99.195155

I. INTRODUCTION

Over the last two decades the design of structured acoustic devices has been strongly influenced by developments in plasmonics and electromagnetic metamaterials, where subwavelength resonators are exploited to achieve unprecedented control of light and enhance light-matter interactions on small scales [1–4]. Building on these ideas, acoustic metamaterials and metasurfaces have been designed to control propagation, localization and attenuation of sound waves in ways previously not thought possible, or even imagined, as in the case of structured materials that negatively refract [5]. Resonators used to realize acoustic metamaterials include traditional Helmholtz and cavity resonators, which have long been used for filtering [6] and sound attenuation [7], as well as membranes, rubber-coated particles and space-coiling structures [5,8,9].

Bubbles, whose acoustic properties have been extensively studied in the context of bubbly liquids [10], biomedical applications [11] and soft-matter physics [12], have also been used to demonstrate a range of phononic-crystal and metamaterial effects underwater [13–20]. Bubbles are especially appealing for this purpose as they support a deeply subwavelength "breathing mode," or Minnaert resonance [21], with the smallness of the resonance frequency linked to the extreme density contrast between air and water [22]. There are, however, challenges in using bubbles for metamaterial applications: beyond their tendency to dissolve, bubble screens and clusters are naturally disordered, mobile, and polydisperse. Such difficulties could be overcome, at the cost of reducing the contrast between the phases, by embedding bubbles in a soft elastic matrix [23–26] or by encapsulating bubbles in elastic shells [27–29].

Given the extraordinary acoustic properties of bubbles, we here suggest to consider superhydrophobic surfaces as natural candidates for realizing highly tunable acoustic metasurfaces. Superhydrophobic surfaces are formed by rough hydrophobic substrates immersed in water, the roughness being either natural or engineered—usually by texturing the substrate with periodic arrays of grooves, pillars or holes [30]. When the roughness varies on a micrometer scale, the immersed substrate may attain a so-called Cassie state, wherein gas bubbles become trapped in the vacancies of the microstructure [31]. Superhydrophobic surfaces are well known for their spectacular fluidic properties, exhibiting anomalous wetting phenomena [31] and reduced hydrodynamic resistance [32]. At the same time, such surfaces naturally provide a planar distribution of subwavelength acoustic resonators, namely, the trapped bubbles. This suggests anomalous scattering and absorption properties, enhanced sound-matter interactions on subwavelength scales and the possibility of guided surface-acoustic "spoof-plasmon" waves [33–35]. We accordingly

envisage superhydrophobic surfaces as acoustic metasurfaces, where the arrangement, shape, and size of the bubble resonators are tuned through the geometry of the trapping microstructure.

Acoustics in bubbly liquids is a classical problem in fluid dynamics (see Ref. [10] and references therein), which has been recently receiving renewed theoretical interest in the context of metamaterials [36–40]. When modeling acoustically forced *trapped* bubbles, however, a modified theoretical framework is required, which couples the equations of acoustics and interfacial fluid mechanics. In particular, friction on the molecular level results in pinning of the bubble menisci, often along the corners of the microstructured cavities. The equilibrium shapes of the trapped bubbles and meniscus boundaries are therefore linked to the geometry of the underlying structure and may accordingly substantially differ from the spherical shape of a free bubble. The pinning conditions also modify the dynamics of the meniscus deformation, which on the micrometer scale are appreciably affected by surface tension. Yet a further complication is that the liquid experiences mixed conditions on the solid-liquid and gas-liquid interfaces, respectively. Our overarching aim is to advance the acoustofluidic modeling of both isolated trapped bubbles and periodic bubble arrays.

There have been several theoretical and experimental studies in the literature of acoustically driven microbubbles trapped in holes, micropits and rectangular cavities, motivated by biological sensing, enhanced cavitation, microfluidic applications, acoustic streaming, as well as the characterization of superhydrophobic surfaces [41–48]. Given the smallness of the trapped bubbles in comparison to the wavelength, these investigations employed an incompressible description, where the subwavelength resonances are damped solely by viscous and thermal dissipation; in that description, the acoustic field enters only as an externally applied uniform-pressure fluctuation, whereas the acoustic scattering is not sought. Such a methodology is adequate when radiation losses are negligible, as one usually expects for micrometer-sized bubbles near resonance [49]. Going beyond single trapped bubbles, Rathgen *et al.* [43] carried out experiments with superhydrophobic surfaces featuring doubly periodic arrays of bubbles trapped in holes; the surfaces were forced by an ultrasound transducer and an averaged meniscus displacement was measured. A pronounced resonant peak was found at a frequency below that predicted for a single isolated bubble. The observed frequency shift was explained by considering the interactions between the trapped bubbles, which in light of the subwavelength periodicity were modeled as quasistatic monopole interactions decaying inversely with distance.

In the above investigations, the trapped bubbles are confined in all three dimensions. In contrast, in this paper our interest is in bubbles trapped in long grooves, a common texture employed for superhydrophobic surfaces. In that case, the bubbles are cylindrical and we expect an essentially different acoustic response. Alluding to studies of cylindrical bubbles [50–52], we anticipate that bubbles trapped in grooves emit cylindrical, rather than spherical, acoustic waves. As a consequence, radiation damping is enhanced and becomes the dominant loss mechanism for bubbles larger than approximately one micrometer [51]. The dominance of radiation damping also implies that the compressibility of the liquid cannot be neglected and an acoustofluidic model is necessary. Finally, interactions between cylindrical trapped bubbles are expected to be markedly different from those between three-dimensional trapped bubbles. Indeed, the pressure disturbance induced by a pulsating cylindrical bubble grows logarithmically on subwavelength scales only to eventually attenuate over distances commensurate with the wavelength. Thus, in contrast to the decaying monopole interactions discussed in Ref. [43], in the case of cylindrical trapped bubbles we expect strong long-range interactions.

In light of the above, we wish to theoretically study the acoustic response of cylindrical bubbles trapped in infinite grooves. Following standard modeling of superhydrophobic surfaces [53,54], we shall assume that the menisci are flat at equilibrium and remain pinned to the corners of the grooves; furthermore, in accordance with the above discussion we ignore viscous and thermal effects. For the sake of simplicity, we shall also assume that the solid substrate is perfectly rigid. We shall first analyze the problem of an isolated trapped bubble subject to a normally incident acoustic plane wave. This two-dimensional problem is formulated in Sec. II. In Secs. III and IV, we systematically develop an asymptotic description of the bubble dynamics and acoustic scattering, based on the smallness of the gas-to-liquid density ratio; our analysis focuses on the resonant long-wavelength regime associated with this limit. Notwithstanding the disparity between the groove size and the wavelength, for cylindrical bubbles it is not possible to entirely neglect the compressibility of the liquid, as already noted. We overcome this difficulty using the method of matched asymptotic expansions [55]; building on the analyses of other long-wavelength scattering problems [22], we match an "inner" bubble-scale near field, where the liquid is approximately incompressible, and an "outer" wavelength-scale acoustic region. In Sec. V, we investigate dilute arrays of trapped cylindrical bubbles, namely, grooved superhydrophobic surfaces; to this end, we use the theory developed for a single isolated trapped bubble, in conjunction with a two-dimensional variant of Foldy's point-scatter approximation and techniques of multiple-scattering theory [56,57]. Concluding remarks are given in Sec. VI.

II. FORMULATION FOR A SINGLE MENISCUS

A. Physical problem

The system considered herein consists of a semi-bounded layer of liquid (density ρ, sound speed c) which is in contact with an infinite hydrophobic wall. The wall, assumed rigid, is decorated with a single groove which is filled with a gas (density $\bar{\rho}$, sound speed $\bar{c}$) in a stable Cassie state. The groove opening is $2a$ and its cross-sectional area is denoted by a^2V. The interfacial tension of the liquid–gas meniscus is denoted by γ. We assume a zero protrusion angle of the meniscus at equilibrium. The values of the liquid and gas pressure at that equilibrium are accordingly identical, say P. Assuming an ideal gas, P is related to $\bar{\rho}$ and $\bar{c}$ via the relation

$$\kappa P = \bar{\rho}\bar{c}^2 \tag{2.1}$$

wherein κ is the gas adiabatic index. Table I(a) presents typical values of the pertinent liquid and gas properties.

The system is excited by an acoustic plane wave (frequency ω, pressure amplitude p_∞) which propagates through the

TABLE I. (a) Typical material values for air-water system. (b) The resulting typical values of the dimensionless parameters.

(a)	
Liquid properties:	
density ρ:	1000 kg m^{-3}
sound speed c:	1500 m s^{-1}
Gas properties:	
density $\bar{\rho}$:	1 kg m^{-3}
sound speed $\bar{c}$:	340 m s^{-1}
adiabatic index κ:	1.4
Liquid-gas properties:	
reference pressure P:	10^5 kg m^{-1} s^{-2}
interfacial-tension coefficient γ:	0.07 kg s^{-2}
(b)	
Material ratios:	
density ratio δ:	10^{-3}
sound-speed ratio χ:	4.4
Geometric parameters:	
scaled area V:	of order unity
Material-geometry parameters:	
stiffness ratio K:	of order $2a$
(with a measured in micrometers)	

liquid towards the wall. In a plane perpendicular to the groove the problem is two-dimensional (2D), see Fig. 1. It is accordingly convenient to employ two unit vectors: $\hat{\boldsymbol{\imath}}$, which is parallel to the wall, and $\hat{\boldsymbol{\jmath}}$, which is perpendicular to the wall, pointing into the liquid.

We assume that p_∞ (and whence the resulting pressure fluctuation) is small compared with both P and γ/a. This assumption allows to linearize both the acoustics and interface dynamics. In the resulting linear framework, it is natural to consider time-harmonic fields with a fixed frequency, say ω. Denoting the position vector by $\mathbf{x}$, it follows that any generic field must possess the form

$$f(\mathbf{x}, t) = \mathrm{Re}[e^{-i\omega t}\hat{f}(\mathbf{x})]. \tag{2.2}$$

In what follows, we conveniently omit the hat decoration; all subsequent variables are therefore phasor quantities. With this convention, the pressure fluctuation associated with the incident plane wave is given by

$$p^{(\mathrm{i})} = p_\infty \exp(-ik\mathbf{x}\cdot\hat{\boldsymbol{\jmath}}), \tag{2.3}$$

where

$$k = \omega/c \tag{2.4}$$

is the wave number in the liquid.

In the linearized description the interfacial boundary conditions are specified on a straight line segment, denoted by $\mathcal{M}$, which coincides with the meniscus at equilibrium. The associated liquid and gas domains are respectively denoted by $\mathcal{L}$ and $\mathcal{G}$. The pressure fluctuations in the liquid and gas domains are respectively denoted by p and $\bar{p}$. They satisfy the Helmholtz equation in both domains,

$$\nabla^2 p + k^2 p = 0 \quad \text{in} \quad \mathcal{L}, \qquad \nabla^2 \bar{p} + \chi^2 k^2 \bar{p} = 0 \quad \text{in} \quad \mathcal{G}, \tag{2.5}$$

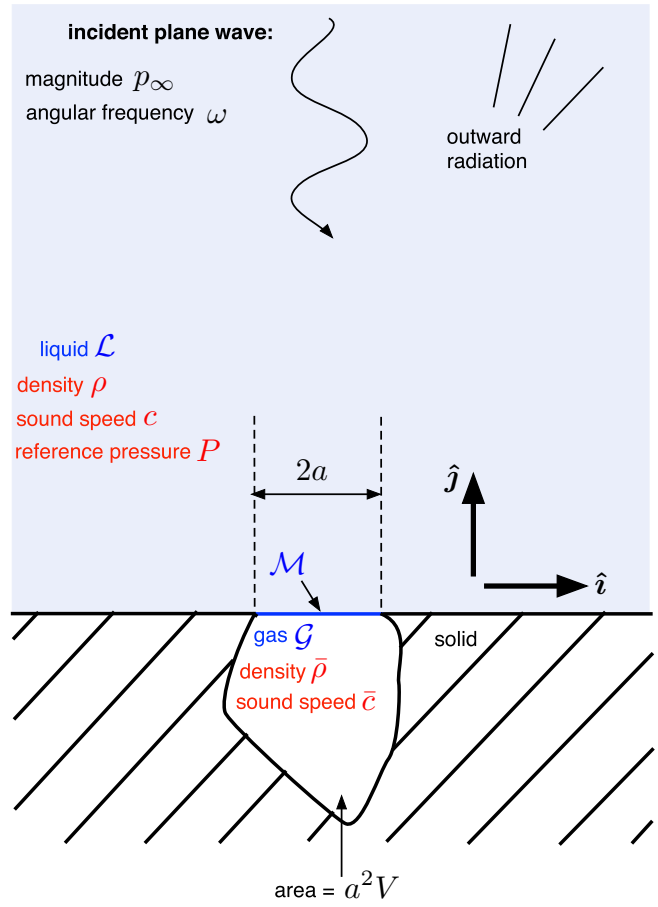

FIG. 1. Schematic of the dimensional problem.

wherein

$$\chi = c/\bar{c} \tag{2.6}$$

is the ratio of sound speeds.

To discuss the boundary conditions we introduce the velocity fluctuations in the respective liquid and gas domains, $\mathbf{u}$ and $\bar{\mathbf{u}}$. These are related to the pressure fluctuations via the linearized momentum equations

$$i\omega\rho\mathbf{u} = \nabla p \quad \text{in} \quad \mathcal{L}, \qquad i\omega\bar{\rho}\bar{\mathbf{u}} = \nabla\bar{p} \quad \text{in} \quad G. \tag{2.7a, b}$$

The boundary $\partial\mathcal{L}$ of the liquid domain consists of the meniscus $\mathcal{M}$ and the solid wall $\partial\mathcal{L}\setminus\mathcal{M}$. Similarly, the boundary ∂G of the gas domain consists of the meniscus $\mathcal{M}$ and the groove boundary $\partial\mathcal{G}\setminus\mathcal{M}$. The impermeability condition at the solid-liquid and solid-gas interfaces in conjunction with (2.7) yields the following Neumann conditions,

$$\hat{\boldsymbol{\jmath}}\cdot\nabla p = 0 \quad \text{on} \quad \partial\mathcal{L}\setminus\mathcal{M}, \qquad \hat{\mathbf{n}}\cdot\nabla\bar{p} = 0 \quad \text{on} \quad \partial\mathcal{G}\setminus\mathcal{M}, \tag{2.8a, b}$$

in which $\hat{\mathbf{n}}$ is a unit vector normal to $\partial\mathcal{G}\setminus\mathcal{M}$.

Consider now the conditions on $\mathcal{M}$. Let s and $\zeta(s)$ respectively denote the rectilinear coordinate along $\mathcal{M}$ and the the normal meniscus displacement (reckoned positive when directed into the liquid). The linearized dynamic condition relates the meniscus curvature to the pressure difference across

$\mathcal{M}$ according to

$$\gamma \frac{d^2\zeta}{ds^2} = p - \bar{p} \quad \text{in} \quad \mathcal{M}. \tag{2.9}$$

Since the meniscus is pinned at its ends to the sharp corners, the displacement is also subject to the end conditions

$$\zeta = 0 \quad \text{on} \quad \partial\mathcal{M}. \tag{2.10}$$

In addition to the dynamic condition we also need to satisfy the linearized kinematic condition, which imposes continuity of the velocity component perpendicular to ∂M; making use of (2.7) this gives

$$\hat{\boldsymbol{\jmath}} \cdot (\nabla \bar{p} - \delta \nabla p) = 0 \quad \text{on} \quad \mathcal{M}, \tag{2.11}$$

wherein

$$\delta = \bar{\rho}/\rho \tag{2.12}$$

is the gas-to-liquid density ratio. Last, relating the flow to the time derivative of the displacement gives, upon making use of (2.7),

$$\hat{\boldsymbol{\jmath}} \cdot \nabla p = \rho\omega^2\zeta \quad \text{on} \quad \mathcal{M}. \tag{2.13}$$

In addition to the above boundary conditions, we require that the scattered field $p - p^{(\mathrm{i})}$ satisfies a radiation condition at large distances from the surface. Since the kinematic conditions (2.11) and (2.13) do not involve the velocity fluctuations, we have obtained a well-posed problem governing p, $\bar{p}$, and ζ. In the preceding description, we have neglected viscosity and heat transfer. Mechanical energy is accordingly lost only by radiation to infinity through wave scattering.

B. Governing parameters and dimensionless formulation

Towards using a dimensionless formulation it is convenient to identify the pertient parameters in the problem. We have already introduced the material ratios χ and δ and the geometric parameter V. A fourth parameter,

$$K = \frac{\kappa P}{\gamma/a}, \tag{2.14}$$

represents the ratio of gas and interface stiffnesses. Note that K depends upon both material and geometric properties; in particular, it is inherently proportional to the size of the groove. Characteristic values of the above parameters, based upon the air-water values of Table I(a), are presented in Table I(b). Since the width $2a$ of realistic grooves in superhydrophobic surfaces is on the micrometer scale, K is of order unity; the cross-sectional area is typically comparable with a^2 and hence V is of order unity. The wave-speed ratio χ is also of order unity. On the other hand, δ is exceedingly small.

In addition to the above parameters we have the acoustic size parameter ka, characterizing the ratio of the wavelength to groove size. With the latter being on the micrometer scale, ka is very small for most of the ultrasound range. Based on the theory of the Minnaert resonance of a free bubble [21], we anticipate a resonance in the subwavelength regime $ka = O(\delta^{1/2})$. This suggests working with the rescaled frequency Ω, defined via

$$ka = \delta^{1/2}\Omega. \tag{2.15}$$

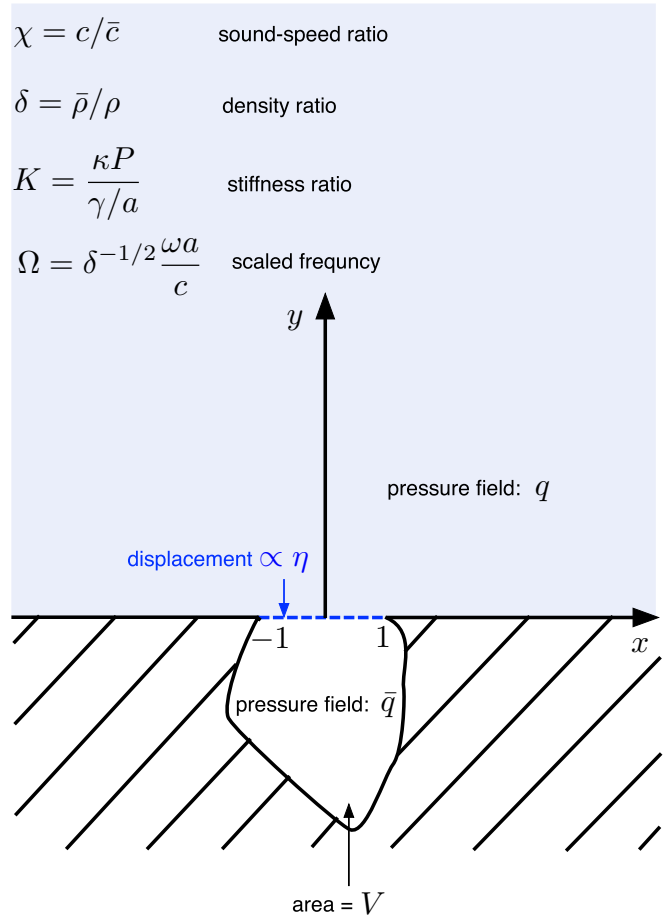

FIG. 2. Schematic of the dimensionless problem.

Writing $\mathbf{x} = ax\hat{\boldsymbol{\imath}} + ay\hat{\boldsymbol{\jmath}}$, we hereafter use the dimensionless Cartesian coordinates (x, y) with the origin at the groove mid-opening, see Fig. 2; we also employ the radial coordinate $r = \sqrt{x^2 + y^2}$. The dimensionless pressure fluctuations and interface displacement are defined as

$$q = \frac{p}{p_\infty}, \quad \bar{q} = \frac{\bar{p}}{p_\infty}, \quad \eta = \frac{\gamma}{a^2 p_\infty}\zeta. \tag{2.16}$$

The Helmholtz equation in the liquid and gas domains respectively reads

$$\frac{\partial^2 q}{\partial x^2} + \frac{\partial^2 q}{\partial y^2} + \delta\Omega^2 q = 0 \quad \text{in} \quad \mathcal{L},$$

$$\frac{\partial^2 \bar{q}}{\partial x^2} + \frac{\partial^2 \bar{q}}{\partial y^2} + \delta\chi^2\Omega^2\bar{q} = 0 \quad \text{in} \quad \mathcal{G}. \tag{2.17a, b}$$

On the solid walls, we have the homogeneous Neumann conditions:

$$\frac{\partial q}{\partial y} = 0 \quad \text{on} \quad \partial\mathcal{L} \setminus \mathcal{M},$$

$$\frac{\partial \bar{q}}{\partial n} = 0 \quad \text{on} \quad \partial\mathcal{G} \setminus \mathcal{M}. \tag{2.18a, b}$$

At the meniscus, the kinematic condition (2.11) becomes

$$\frac{\partial \bar{q}}{\partial y} = \delta\frac{\partial q}{\partial y} \quad \text{on} \quad \mathcal{M}. \tag{2.19}$$

In addition, upon making use of (2.1) we obtain from (2.13)

$$\frac{\partial q}{\partial y} = K\chi^2\Omega^2\eta \quad \text{on} \quad \mathcal{M}, \tag{2.20}$$

which introduces a coupling to the displacement η. The latter is governed by the dynamic condition and the pinning constraint [cf. (2.9)–(2.10)],

$$\frac{d^2\eta}{dx^2} = q - \bar{q} \quad \text{on} \quad \mathcal{M}, \quad \eta = 0 \quad \text{at} \quad \partial\mathcal{M}. \tag{2.21a, b}$$

In the dimensionless notation, the incident wave is

$$q^{(\mathrm{i})} = \exp\{-i\delta^{1/2}\Omega y\}. \tag{2.22}$$

Conditions (2.18)–(2.21) are supplemented by a radiation condition which is imposed at large y on the scattered wave $q - q^{(\mathrm{i})}$.

Note that integration of (2.17b) in conjunction with Gauss's theorem yields, upon making use of (2.18b)–(2.19),

$$\int_{-1}^{1} \left.\frac{\partial q}{\partial y}\right|_{y=0} dx + \chi^2\Omega^2 \iint_{\mathcal{G}} \bar{q}\, dx\, dy = 0. \tag{2.23}$$

While this constraint does not provide any independent information, its use simplifies the asymptotic analysis that follows.

III. LONG-WAVELENGTH LIMIT

Given the smallness of δ, we now focus upon the asymptotic limit

$$\delta \ll 1, \quad \Omega \text{ fixed}, \tag{3.1}$$

which, with (2.15), corresponds to a long-wavelength regime; this regime is characterized by two disparate length scales, namely, $O(1)$ and $O(\delta^{-1/2})$, which in the dimensional description respectively correspond to the groove size a and wavelength $2\pi/k$. In what follows, the singular limit (3.1) is handled using matched asymptotic expansions [22]. The "inner" region in these expansions represents the "near-field" acoustics, while the "outer" region describes the incident, reflected and diffracted fields. Our interest is in the leading-order description in both of these regions. In particular, asymptotic matching is expected to provide the relation between the outer acoustic response and the meniscus and gas-pressure dynamics. As is often the case in asymptotic analyses of long-wavelength scattering processes, the expansions we find contain terms logarithmic in the small parameter δ. We shall follow the standard approach [55,58] of grouping together logarithmically separated terms, ensuring an asymptotic error that is "algebraically small" (i.e., smaller than some power of δ).

A. Inner region

We shall start by considering the inner region where the coordinates x, y are $O(1)$. In the gas domain, the pressure field $\bar{q}$ satisfies Laplace's equation at leading order, see (2.17b). Given (2.18b)–(2.19), $\bar{q}$ additionally satisfies at leading order a homogeneous Neumann condition over the entire boundary $\partial\mathcal{G}$. It follows that $\bar{q}$ is uniform at that order. The integral relation (2.23) provides the constant value of $\bar{q}$ as

$$\bar{q} = -\frac{\mathcal{F}}{\chi^2\Omega^2 V}, \tag{3.2}$$

in which

$$\mathcal{F} = \int_{-1}^{1} \left.\frac{\partial q}{\partial y}\right|_{y=0} dx \tag{3.3}$$

is proportional to the volumetric flux (per unit length in the z direction) emanating from the meniscus. In Appendix A, we show that the preceding results coincide with those obtained using a "thermodynamic" description of the bubble.

In the liquid, the pressure also satisfies Laplace's equation at leading order, see (2.17a):

$$\frac{\partial^2 q}{\partial x^2} + \frac{\partial^2 q}{\partial y^2} = 0 \quad \text{for} \quad y > 0. \tag{3.4}$$

In addition, it satisfies (2.18a) and (2.20)–(2.21), which retain their form at leading order. Since the radiation condition does not apply in the inner region, conditions at infinity follow instead from matching with the outer pressure. To this end, note that Laplace's equation in conjunction with (2.18a) and (3.3) implies a 2D sourcelike behavior at large distances, namely

$$q \sim \frac{\mathcal{F}}{\pi} \ln r \quad \text{as} \quad r \to \infty. \tag{3.5}$$

Last, we observe that both q and η are even functions of x. This symmetry, which follows from $\bar{q}$ being uniform, does not necessarily hold at higher asymptotic orders.

B. Canonical inner problem

The inner problem is closed apart from the unknown value of $\mathcal{F}$. The dependence upon that constant can actually be factored out by defining

$$q - \bar{q} = \mathcal{F}\tilde{q}, \quad \eta = \mathcal{F}\tilde{\eta}, \tag{3.6}$$

where $\tilde{q}$ and $\tilde{\eta}$ respectively represent the rescaled excess liquid pressure and meniscus displacement. The leading-order inner problem governing $\tilde{q}$ consists of (i) Laplace's equation,

$$\frac{\partial^2 \tilde{q}}{\partial x^2} + \frac{\partial^2 \tilde{q}}{\partial y^2} = 0 \quad \text{for} \quad y > 0; \tag{3.7}$$

(ii) the homogeneous Neumann condition at $y = 0$ [cf. (2.18a)]

$$\frac{\partial \tilde{q}}{\partial y} = 0 \quad \text{for} \quad |x| > 1; \tag{3.8}$$

(iii) the inhomogeneous condition at $y = 0$ [cf. (2.20)]

$$\frac{\partial \tilde{q}}{\partial y} = K\chi^2\Omega^2\tilde{\eta} \quad \text{for} \quad |x| < 1; \tag{3.9}$$

and (iv) the far-field condition [cf. (3.5)]

$$\tilde{q} \sim \frac{1}{\pi} \ln r \quad \text{as} \quad r \to \infty; \tag{3.10}$$

note that the solvability condition (3.3) now reads

$$\int_{-1}^{1} \left.\frac{\partial \tilde{q}}{\partial y}\right|_{y=0} dx = 1. \tag{3.11}$$

Condition (3.9) introduces the coupling to the interface displacement, itself governed by [cf. (2.21)]

$$\frac{d^2\tilde{\eta}}{dx^2} = \tilde{q}|_{y=0} \quad \text{for} \quad |x| < 1; \quad \tilde{\eta} = 0 \quad \text{at} \quad x = \pm 1. \tag{3.12}$$

The canonical problem which results from factoring out the flux $\mathcal{F}$, as prescribed by (3.7)–(3.12), is self-contained. In fact, since the gas pressure does not appear in that problem, $\tilde{q}$ and $\tilde{\eta}$ depend upon a *single* dimensionless group, namely,

$$\lambda = K\chi^2\Omega^2. \tag{3.13}$$

Making use of definitions (2.4), (2.6), (2.12), (2.14) in conjunction with (2.1), the above group is readily expressed in terms of the pertinent dimensional quantities

$$\lambda = \frac{\rho\omega^2 a^3}{\gamma}. \tag{3.14}$$

If follows that the canonical inner problem is independent of the properties of the gas and the area of the groove.

Once $\tilde{q}$ and $\tilde{\eta}$ are determined, obtaining the unscaled variables q and η merely requires the calculation of the unknown flux $\mathcal{F}$; as we shall see, the latter is determined by asymptotic matching with the outer region. To that end, we note that (3.10) can be refined to

$$\tilde{q} \sim \frac{1}{\pi}\ln(2r) + \beta + o(1) \quad \text{for} \quad r \gg 1. \tag{3.15}$$

(The 2 factor is introduced for convenience and merely amounts to a specific definition of the parameter β.) The constant β is determined from the solution of the canonical problem. As such, it is a function of λ alone. As will become evident, β captures the dynamical response of the quasistatic inner region.

Since the canonical problem is driven by the inhomogeneous condition (3.10), which involves a real-valued forcing, both $\tilde{q}$ and $\tilde{\eta}$ are real-valued (and whence so is β). On the other hand, with $\mathcal{F}$ generally being complex-valued, so are q and η.

C. Outer region

The outer region, at $O(\delta^{-1/2})$ distances, is described using the stretched coordinates,

$$X = \delta^{1/2}\Omega x, \quad Y = \delta^{1/2}\Omega y, \quad R = \delta^{1/2}\Omega r. \tag{3.16}$$

Writing $q(x, y) = Q(X, Y)$, we find from (2.17a) that at leading order Q satisfies the Helmholtz equation,

$$\frac{\partial^2 Q}{\partial X^2} + \frac{\partial^2 Q}{\partial Y^2} + Q = 0. \tag{3.17}$$

At the boundary $Y = 0$ the groove shrinks to the point $X = 0$. It therefore follows from (2.18a) that Q satisfies the homogeneous Neumann condition virtually on the entire X axis,

$$\frac{\partial Q}{\partial Y} = 0 \quad \text{for} \quad X \neq 0. \tag{3.18}$$

In addition, it satisfies matching with the inner solution in the limit $R \to 0$, together with the radiation condition, associated with the imposed incident wave [cf. (2.22)]

$$Q^{(\mathrm{i})} = e^{-iY}. \tag{3.19}$$

It is illuminating to consider for a moment the outer solution that would hold in the absence of any meniscus. It is simply obtained by ignoring the matching requirement, and accordingly consists of the incident wave (3.19) together with a reflected wave which is determined by the radiation condition and the boundary condition at $Y = 0$. For the homogeneous condition (3.18), the reflected wave

$$Q^{(\mathrm{r})} = e^{iY} \tag{3.20}$$

is in phase with the incident wave. The solution thus consists of the sum

$$Q^{(\mathrm{i})} + Q^{(\mathrm{r})} = 2\cos Y. \tag{3.21}$$

With a meniscus present, the need for asymptotic matching results in an origin singularity in the outer solution. The isotropic behavior (3.5) suggests, in turn, isotropic diffraction and hence a fundamental solution of the Helmholtz equation. The radiation condition therefore necessitates a solution of the form

$$Q = 2\{\cos Y + A\mathcal{H}_0(R)\}, \tag{3.22}$$

wherein the last term, in which $\mathcal{H}_0$ denotes the Hankel function of the first kind and order zero, represents an outward-propagating cylindrical wave. The integration constant A accordingly represents the scattering coefficient of the groove. It may be noted at this stage that our neglect of intrinsic losses implies the constraint

$$\mathrm{Re}\{A\} = -|A|^2; \tag{3.23}$$

this constraint follows from an energy balance which is independent of the specific scatterer (see, e.g., Ref. [57]).

Towards asymptotic matching, we make use of the small-argument asymptotic expansion of the Hankel function [22] to obtain

$$Q \sim 2 + \frac{4i}{\pi}A\left(\ln R + \gamma_{\mathrm{E}} - \ln 2 - \frac{\pi i}{2}\right) + O(R^2\ln R) \quad \text{as} \quad R \to 0, \tag{3.24}$$

where $\gamma_{\mathrm{E}} \approx 0.5772\ldots$ is the Euler–Mascheroni constant. Matching with (3.15) we find, upon comparing the logarithmically growing terms,

$$\mathcal{F} = 4iA. \tag{3.25}$$

Then, matching the constant terms and using (3.25) gives the amplitude of the monopole term in (3.22) as

$$A = \frac{i\pi}{\ln(\Omega^2\delta/16) + 2\gamma_{\mathrm{E}} - 2\pi\beta(\lambda) + 2\pi(\chi^2\Omega^2 V)^{-1} - i\pi}. \tag{3.26}$$

As mentioned before, we allow for a logarithmic dependence upon δ in the leading-order term; given (3.25), this dependence applies in the inner region as well. It is notable that the form (3.26) is consistent with the energy balance (3.23).

We have accordingly obtained the two quantities of interest, namely, the flux $\mathcal{F}$ and the scattering coefficient A. These quantities depend upon the function $\beta(\lambda)$, which we now discuss.

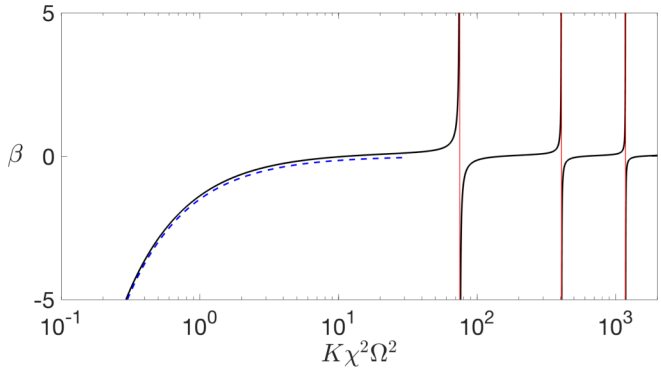

FIG. 3. Variation of β with $\lambda = K\chi^2\Omega^2$: solid line: exact solution; dashed line: strong interfacial-tension approximation (3.27); thin vertical lines: antiresonances

D. The function $\beta(\lambda)$

The function $\beta(\lambda)$ is determined in Appendix B by solving the canonical inner problem (3.7)–(3.12) using elliptical cylinder coordinates. Figure 3 presents the resulting variation of β with $\lambda = K\chi^2\Omega^2$. This exact variation is depicted by the solid line. We note several features of this function that are derived in Appendix B. First, at small values of the argument β diverges,

$$\beta \sim -\frac{3}{2\lambda} \quad \text{for} \quad \lambda \ll 1; \tag{3.27}$$

this approximation is portrayed by the dashed line in Fig. 3. In this limit, the meniscus is parabolic, with

$$\tilde{\eta} \sim \frac{3(1-x^2)}{4\lambda}. \tag{3.28}$$

We next note that β has an infinite sequence of singularities at discrete values of its argument, the first three of these being indicated by the vertical lines in Fig. 3. Let Δ be the difference between the argument and one of these singular values, say λ_a; then, according to the analysis in Appendix C,

$$\beta \sim -\frac{\text{constant}}{\Delta} \quad \text{for} \quad |\Delta| \ll 1, \tag{3.29}$$

where the constant is positive; it follows that $\beta \to \infty$ when λ approaches λ_a from below, while $\beta \to -\infty$ when λ approaches λ_a from above. This is indeed observed in Fig. 3. Last, in Appendix B, we confirm that for large values of the argument, but away from the singularities, $\beta = o(1)$.

E. Illustrations

With the variation $\beta(\lambda)$ available, the response of the single bubble to the planar wave is provided by formula (3.26). In what follows we illustrate this formula employing the values $\delta = 10^{-3}$, $\chi = 4.4$, and $V = 1$ [see Table I(b)]; these values are used hereafter throughout. Taking P as the atmospheric pressure we find that, with a measured in micrometers, K is approximately $2a$; for micrometer-size grooves it is of order unity.

In Fig. 4 we plot the variation of $|A|$ and $\arg A$ with Ω for $K = 1$. In the evaluation of A using (3.26) we have calculated β using both the exact solution, as outlined in Appendix B, and the small-$K\chi^2\Omega^2$ approximation (3.27); the resulting values of A obtained by these two calculations are respectively portrayed in solid and dashed curves. We observe resonances, where $|A|$ attains a local maxima, as well as antiresonances, where $|A|$ vanishes. The loci of the resonances and antiresonances in the (Ω, K) plane are shown in Fig. 5. The larger is the value of K, the earlier do the antiresonances occur on the Ω axis. We also observe that the fundamental resonance occurs on that axis before the first antiresonance, while higher-order resonances closely follow the antiresonances.

The appearance of antiresonances is evidently related to the singularities of β. Indeed, when $|\beta| \to \infty$, we find from

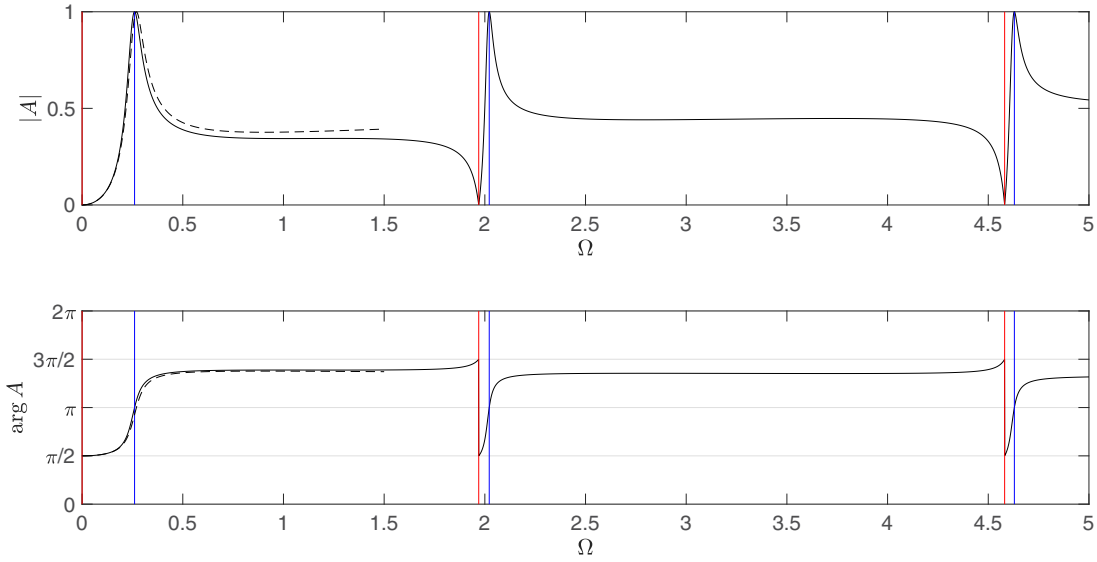

FIG. 4. The magnitude and phase of A as functions of Ω for $K = 1$. The solid curves are obtained using the exact variation of β with $K\chi^2\Omega^2$, while the dashed curves are obtained using the small-$K\chi^2\Omega^2$ approximation (3.27). The vertical lines indicate the values of the resonance frequencies, obtained using (4.1), and antiresonance frequencies, obtained using (B18) and (C1).

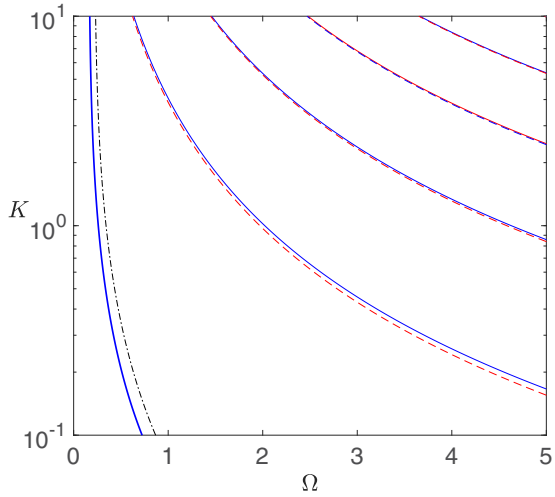

FIG. 5. Loci in the (Ω, K) plane of the resonances (solid lines) and antiresonances (dashed lines) of a single trapped bubble. The dash-dotted line shows approximation (4.4) for the fundamental resonance.

(3.26) that $A \to 0$. However, the appearance of resonances and antiresonances in pairs requires some explanation.

IV. RESONANCES AND ANTIRESONANCES

A. Resonance frequencies

Considering (3.26) we see that the maximum possible amplitude of A is obtained whenever the real part of the denominator vanishes. This gives damped resonances at frequencies Ω_r satisfying:

$$\beta(K\chi^2\Omega_r^2) = \frac{\gamma_E}{\pi} + \frac{1}{2\pi}\ln\frac{\Omega_r^2\delta}{16} + \frac{1}{V\chi^2\Omega_r^2}. \tag{4.1}$$

At any one of these resonance we find from (3.26) that

$$A(\Omega_r) = -1. \tag{4.2}$$

In particular, the amplitude $|A(\Omega_r)| = 1$, independently of material properties.

Given the formal largeness of $\ln\delta$, there are two ways to satisfy the resonance conditions. The first, which corresponds to the fundamental resonance, applies for small frequencies, where (3.27) applies and (4.1) reduces to

$$-\frac{3}{2K\chi^2\Omega_r^2} \sim \frac{\ln\delta}{2\pi} + \frac{1}{V\chi^2\Omega_r^2}, \tag{4.3}$$

which gives

$$\Omega_r^2 \sim \frac{\pi(3/K + 2/V)}{\chi^2\ln(1/\delta)}, \tag{4.4}$$

corresponding to "logarithmically small" frequencies. Recalling that the limit (3.27) is accompanied by the approximately parabolic profile (3.28), and substituting the resonance value [obtained from (3.25) and (4.2)]

$$\mathcal{F} = -4i \tag{4.5}$$

yields

$$\eta \sim -\frac{3i(1-x^2)}{K\chi^2\Omega^2}. \tag{4.6}$$

The approximation (4.4) for the fundamental resonance is depicted by the dash-dotted line in Fig. 5. While the approximation agrees qualitatively with the exact frequencies calculated using (4.1), the error is substantial; indeed, the error in (4.4) can be shown to be $O(\ln\ln\frac{1}{\delta}/\ln^2\frac{1}{\delta})$.

An essentially different balance, at nonsmall frequencies, has to do with the singularities of β, which correspond to antiresonances at discrete frequencies $\{\Omega_a\}$. Close to these singularities β is large, provided by (3.29). Balancing with the $\ln\delta$ term in (4.1) implies that the higher-order resonance frequencies are formally close to the antiresonances, with

$$\Omega_r - \Omega_a \sim \frac{\text{constant}}{\ln(1/\delta)}, \tag{4.7}$$

where positivity of the constant here follows from (3.29). This explains the "attraction" of the higher-order resonances to the antiresonances, as observed in Figs. 4 and 5.

With the rescaled pressure $\tilde{q}$ being real-valued, and given (4.5), the unscaled pressure q is imaginary at resonance; the same holds for the displacement. In Fig. 6, we present the contour maps of the imaginary part of $q(x, y)$ at the frequencies of the "zeroth-order" (fundamental) and "first-order" resonances, as obtained for $K = 1$. Also shown are the corresponding imaginary parts of the displacements. For convenience, these are plotted on the same axes used to portray the pressure map; since the displacements have not been normalized by a [recall (2.16)], the latter plots only

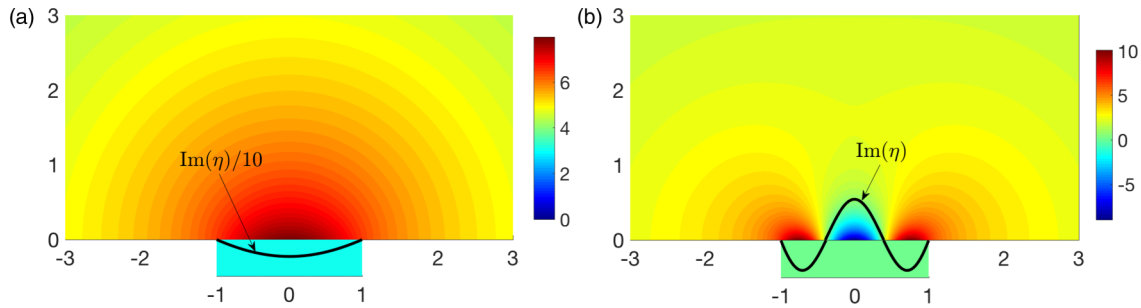

FIG. 6. Contour maps of the imaginary part of $q(x, y)$ at resonance for $K = 1$ (cf. Fig. 4). (a) Zeroth-order resonance, $\Omega = 0.26$. (b) First-order resonance, $\Omega = 2.02$. Also shown is the imaginary part of η. The small rectangles, of unity area, indicate the gas cavity; their color corresponds to the (imaginary part of) gas-domain pressure value, Im $\bar{q}$.

provide a relative measure. Notwithstanding the above, it is worth noting that the displacement is about ten times larger at the zeroth-order resonance than at the first-order resonance. Note that at the fundamental resonance the displacement is parabolic, as predicted in (4.6).

B. Antiresonances

We next consider the antiresonances, namely, the set of frequencies $\{\Omega_a\}$ where the scattering coefficient A vanishes; note that the flux $\mathcal{F}$ and hence the gas pressure fluctuation $\bar{q}$ also vanish at these frequencies [see (3.2) and (3.25)]. Interestingly, we also find from (2.20) and (3.3) that the mean displacement vanishes

$$\int_{-1}^{1} \eta(x)\, dx = 0. \tag{4.8}$$

The liquid pressure in the inner region, however, does not vanish; nor does the meniscus displacement. In fact, since the antiresonance frequencies correspond to the singularities of β, which implies in turn that $\tilde{q}$ is unbounded, it may at first appear that these diverge at these frequencies. Rather, the true liquid pressure $q = \mathcal{F}\tilde{q}$ remains finite since the product $\mathcal{F}\beta \to 2$ as any of the antiresonances are approached [see indeed (3.25)–(3.26)]. Thus the unscaled pressure field in the inner region satisfies

$$q \to 2 \quad \text{as} \quad r \to \infty. \tag{4.9}$$

The latter is the inner-region value of the sum (3.21) of the incident and reflected pressure fields. Thus at antiresonance the action of the incident pressure on the meniscus is precisely balanced by the capillary stresses and the coupling between the meniscus dynamics and the liquid pressure in the inner region. The gas bubble is idle and plays no role in this balance; as a consequence there is no scattering: even though the liquid pressure and meniscus are oscillating, the bubble is acoustically invisible in the outer region, producing no signal. Indeed, since the antiresonances are determined from the singularities of β, they can only depend upon the group (3.13) which is independent of the gas properties (namely, $\bar{\rho}$ and $\bar{c}$) and the groove area [recall (3.14)]. With the gas being idle, it is hardly surprising that its properties are not manifested.

Since the unscaled pressure q is forced at antiresonance by the real-valued condition (4.9), it must be real-valued as well. To further illustrate the above deductions we show in Fig. 7 the contour maps of $\mathrm{Re}(q)$ at the first-order antiresonance ($\Omega \approx 1.97$, cf. Fig. 4) for $K = 1$. Note the zero mean displacement, in agreement with (4.8), and the idle gas pressure.

The antiresonance frequencies can be determined directly by considering the canonical inner problem with zero flux. There are nontrivial solutions to this problem only for certain special frequencies, $\Omega = \{\Omega_a\}$, which constitute the eigenvalues of that problem. The elliptic-cylinder coordinates scheme of Appendix B is adapted in Appendix C to solve this eigenvalue problem. The resulting discrete values of Ω_a, obtained for the appropriate K values, are indicated in Figs. 4 and 5.

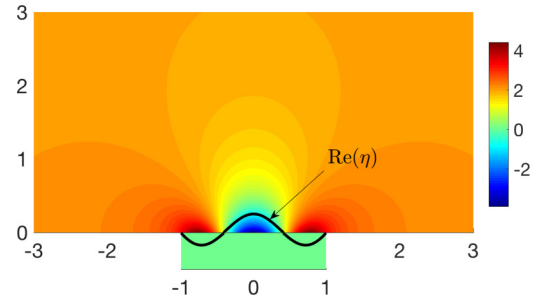

FIG. 7. Contour maps of the real part of $q(x, y)$ at the first-order antiresonance for $K = 1$. Also shown is the real part of η. The small rectangle indicates the corresponding gas-domain pressure value $\mathrm{Re}(\bar{q})$.

V. DILUTE ARRAYS OF TRAPPED BUBBLES

A. Foldy's approximation

Consider now a more complex configuration where the solid surface is decorated not with one but rather with an equally spaced array of identical grooves. For subwavelength grooves, $ka \ll 1$, and in the "dilute" limit where the array spacing L is large in comparison with a, Foldy's approximation [56,57] allows us to build on the theory we have developed for a single groove to study the response of the array. Foldy's method, which has been widely used to study clusters and arrays of free bubbles, among other applications, holds for dilute collections of subwavelength scatterers that radiate isotropically and in proportion to the local value of the pressure field (excluding the self-scattering). In the present case, the proportionally constant, or scattering coefficient, is provided by the complex amplitude A studied in the preceding sections; we may accordingly consider A as a known function of Ω, provided by (3.26), which encodes both the near field and acoustic properties of a single trapped bubble and in particular describes its multiple resonances and antiresonances. We note that the outer description (3.22) coincides with Foldy's approximation in the case of a single groove; the effective pressure acting on that groove is given by the superposition of the incident and reflected plane waves, evaluated at the groove's position. For a dilute array of grooves, the external pressure acting on any given groove is also affected by the cylindrical waves emitted by all the other grooves. Foldy's scheme thereby approximately accounts for all the multiple-scattering events between the bubbles in the array.

Foldy's approximation can only be applied when $ka \ll 1$ and $L/a \gg 1$. The product of these numbers, $l = kL$, remains otherwise arbitrary. In fact, this product represents the ratio between the period L and the wavelength $2\pi/k$. Recalling (2.15), we note that l is related to the dimensionless frequency Ω via

$$l = \delta^{1/2}\frac{L}{a}\Omega, \tag{5.1}$$

where the representation by a product of a small parameter and a large one is evident. In what follows we shall apply Foldy's scheme to an array of grooves, focusing on both infinite and finite arrays.

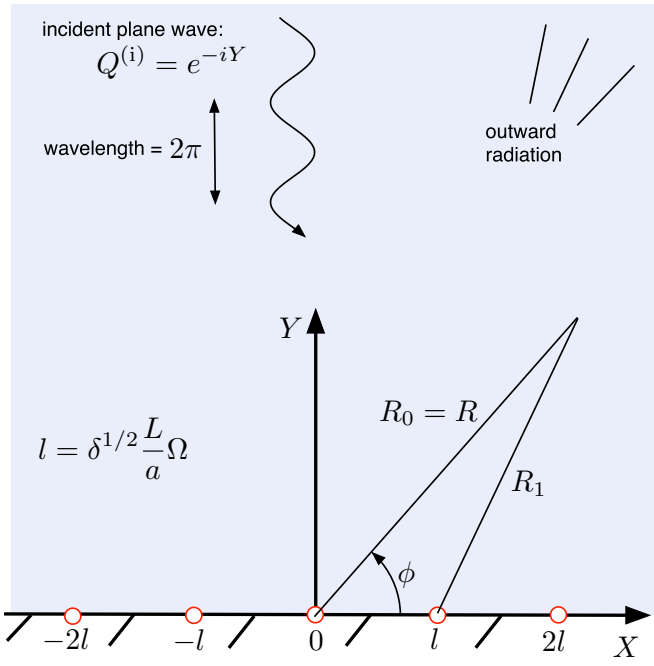

FIG. 8. Dimensionless schematic of a dilute array of trapped bubbles.

B. Infinite arrays

Consider first the case of an infinite periodic array of grooves. It is convenient to analyze scattering from the array using the outer stretched coordinates [cf. (3.16)], where lengths are normalized by $1/k$, so that the wavelength is 2π and the dimensionless period is l, see Fig. 8. Let the positions of the grooves be $(X, Y) = (X_n, 0)$, where $X_n = nl$ and $n = -\infty, \ldots, \infty$. As before, we assume an incident plane wave propagating towards the surface [cf. (3.19)]. In that case, symmetry dictates that the grooves emit cylindrical waves in tutti; thus the total field is

$$Q = 2\cos Y + 2w \sum_{n=-\infty}^{\infty} \mathcal{H}_0(R_n), \tag{5.2}$$

where $R_n = \sqrt{(X - X_n)^2 + Y^2}$ is the radial distance from the nth groove (see Fig. 8) and the complex amplitude w remains to be determined. Note that (5.2) is consistent with the Neumann condition applying on $Y = 0$ for $X \neq nl$. Following Foldy's scheme, the scattering coefficient A times the external field acting on an arbitrary groove, say the mth one, must equal $2w$ [cf. (3.22)]:

$$\left[1 + w \sum_{n\neq m} \mathcal{H}_0(|n-m|l)\right] A = w \quad \forall m \in \mathbb{Z}. \tag{5.3}$$

The dependence upon the arbitrary index m is readily eliminated from (5.3); indeed, defining the lattice sum

$$\sigma(l, \mathcal{K}) = \sum_{n\neq 0} e^{in\mathcal{K}l} \mathcal{H}_0(|n|l), \tag{5.4}$$

where $\mathcal{K} \in [0, \pi/l]$, we find that (5.3) can be written as

$$[1 + w\sigma(l, 0)]A = w. \tag{5.5}$$

The additional dependence upon $\mathcal{K}$ in (5.4) is not needed here but will be useful later. Solving for w, we find

$$w = \frac{A}{1 - A\sigma(l, 0)}. \tag{5.6}$$

Following Linton [59], the lattice sum (5.4) is calculated by transforming the conditionally convergent series into the absolutely convergent series

$$\sigma(l, \mathcal{K}) = -1 - \frac{2i}{\pi}\left(\gamma_{\mathrm{E}} + \ln\frac{l}{4\pi}\right) - \frac{2i}{h_0} - 2i\sum_{n\neq 0}\left(\frac{1}{h_n} - \frac{1}{2\pi|n|}\right), \tag{5.7}$$

where

$$h_n = \begin{cases} \sqrt{(\mathcal{K}l + 2\pi n)^2 - l^2}, & |\mathcal{K}l + 2\pi n| \geqslant l \\ -i\sqrt{l^2 - (\mathcal{K}l + 2\pi n)^2}, & |\mathcal{K}l + 2\pi n| < l \end{cases}. \tag{5.8}$$

The coefficient w directly determines the near fields of the scatterers. Specifically, each of these near fields is described by the single-groove canonical problem discussed in Sec. III, the only exception being that the scaling prefactor, the flux $\mathcal{F}$, is no longer proportional to A via (3.25); rather, $\mathcal{F} = 4iw$, where w depends on A via (5.6). In particular, w (rather than A) is now proportional to the gas-pressure fluctuation. It is evident from (5.6) that the near fields exhibit antiresonances at precisely the same frequencies as an isolated groove, whereas the resonances are modified by groove-groove interactions.

The solution for w also allows, via (5.3), the calculation of the pressure field at distances large compared with the groove size. Of particular interest is the far-field, i.e., distances from the surface large compared with the wavelength. Using the asymptotic relation (see [59])

$$\sum_{n=-\infty}^{\infty} \mathcal{H}_0(R_n) \sim \frac{2}{l} \sum_{n=-\lfloor l/2\pi \rfloor}^{\lfloor l/2\pi \rfloor} \frac{e^{i(2n\pi X/l + Y\sqrt{1-(2n\pi/l)^2})}}{\sqrt{1-(2n\pi/l)^2}} \quad \text{as} \quad Y \to \infty, \tag{5.9}$$

we find from (5.3) that the scattered far field consists of one or more plane waves, depending on the largeness of l. In particular, when the spacing is smaller than one wavelength, i.e., for $l < 2\pi$, there is only a single reflected wave:

$$Q \sim e^{-iY} + \mathcal{R}e^{iY} \quad \text{as} \quad Y \to \infty, \tag{5.10}$$

wherein

$$\mathcal{R} = 1 + \frac{4w}{l} \tag{5.11}$$

is a complex-valued reflection coefficient. In the absence of dissipation, energy conservation clearly requires that $|\mathcal{R}| = 1$; this is confirmed by substituting (5.6) into (5.11), using the single-groove energy balance (3.23) and $\mathrm{Re}(\sigma(l, 0)) = -1 + 2/l$.

To present the above results we employ the values which have been used throughout in the analysis of a single groove, namely, $\delta = 0.001$ and $V = 1$, as well as the value $K = 1$.

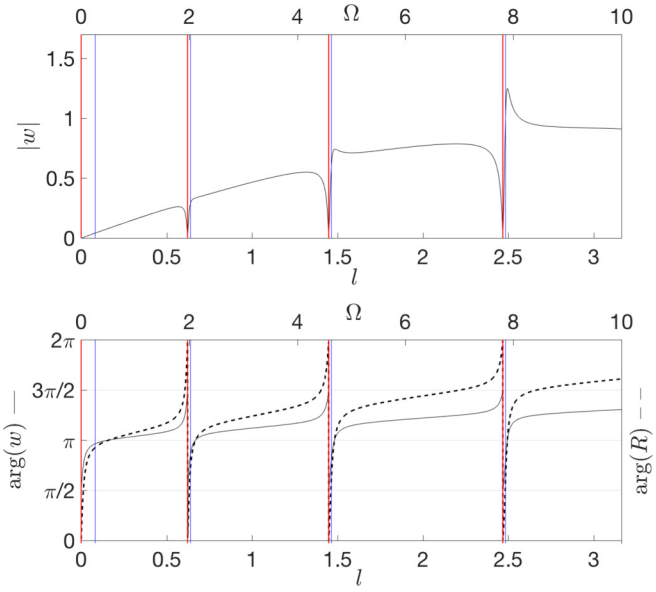

FIG. 9. Infinite array of grooves: $|w|$, $\arg w$, and $\arg R$ as functions of l (or Ω) for $L/a = 10$ and $K = 1$. The vertical lines indicate the corresponding single-groove resonance frequencies, obtained using (4.1), and antiresonance frequencies, obtained using (B18) and (C1).

We focus on the case where the spacing is small compared to the wavelength. In this regime, which is relevant to grooved superhydrophobic surfaces, the interaction of any two grooves grows logarithmically, rather than attenuates, with the distance between them; the interaction only attenuates over distances comparable to the wavelength.

With δ fixed, the above requirement of small l implies that L/a cannot be too big, see (5.1). To illustrate how these strong long-range interactions affect the response we set $L/a = 10$, for which $l/\Omega \approx 0.3$. Figure 9 shows the variation of $|w|$, $\arg w$, and $\arg R$ with l (or Ω). It clearly confirms our prediction of the robustness of the single-groove antiresonances, indicated in the usual manner by vertical lines. The single-groove resonances, on the other hand, are significantly modified. Up to around the second antiresonance, $|w|$ varies essentially linearly with l, except close to the first antiresonance; the zeroth and first resonances are entirely suppressed. There are still clear signatures, however, of these isolated-groove resonances in the phases $\arg w$ and $\arg R$. In particular, close to the fundamental single-groove resonance and between each two antiresonances, there is a frequency for which $\arg R = \pi$ (i.e., $R = -1$) and the surface effectively reflects as if it were acoustically soft (rather than rigid as the underlying substrate).

C. Long-finite arrays

In reality, superhydrophobic surfaces are finite. Naively, it seems plausible that long-finite arrays, consisting of a large number of grooves, behave similarly to infinite arrays. When the spacing is deeply subwavelength, however, the length of the whole array may still be smaller than one wavelength; this, together with the long-range character of the groove-groove interactions, suggests conducting a comparison between long-but-finite and infinite arrays.

To this end, consider a finite array of $2N + 1$ ($N \in \mathbb{N}$) grooves that are distributed evenly about $X = 0$, *viz.*, $X_n = nl$, where $n = -N, \ldots, N$. In this case, which lacks the translational invariance of an infinite array, the total wave field is [cf. (5.2)]

$$Q = 2\cos Y + 2\sum_{n=-N}^{N} w_n \mathcal{H}_0(R_n), \tag{5.12}$$

where the coefficients $\{w_n\}$ remain to be determined. From (5.12), Foldy's scheme is developed similarly to the infinite case [cf. (5.3)], giving

$$\left[1 + \sum_{n\neq m} w_n \mathcal{H}_0(|n-m|l)\right] A = w_m \quad \text{for} \quad m = -N, \ldots, N. \tag{5.13}$$

This is an elementary matrix problem for $\{w_n\}$. Note that symmetry implies $w_n = w_{-n}$ and hence only a system of $N + 1$ equations needs to be solved.

In Fig. 10, we compare the variation with l of the coefficient $|w_0|$, calculated by numerically solving (5.13) for $N = 20$, and that of the coefficient $|w|$ ($= |w_0|$), which corresponds to an infinite array [cf. (5.6)]. In both cases, we have set $L/a = 10$. The response of the finite array is essentially identical to that of the infinite one, expect in a sequence of frequency intervals wherein the response of the finite array oscillates wildly. The first such interval is relatively wide and is positioned about the fundamental resonance frequency of an isolated groove; subsequent intervals are narrower, and are positioned about the higher-order resonances of a single groove. We have numerically verified that, within the above frequency intervals, the response of the finite array does not approach that of the infinite one with increasing N. This observation is rationalized next.

D. Surface waves

The above observations strongly suggest that arrays of bubbles trapped in the grooves of a rigid substrate are capable of guiding surface waves, namely, waves which propagate along the surface and attenuate exponentially fast in the normal direction. Indeed, such waves would only be excited in the finite case, by diffraction of the incident plane wave at the edges of the array. In the absence of dissipation, surface waves propagate without attenuation and hence the grooves would interact across arbitrary distances. Moreover, counter-propagating surface waves may form standing waves along the finite array, resulting in resonances limited only by diffraction of the surface waves at the edges (similar to so-called optical Fabry-Pérot resonances [60]). Multiple resonances are indeed visible in Fig. 11, which zooms in on the first oscillatory frequency interval in Fig. 10. A similar effect has been previously observed in a different scenario, of plane-wave scattering from an array of (nonresonant) rigid cylinders [61,62].

The existence of surface waves in the present case is hardly surprising. While flat solid surfaces are incapable of supporting surface waves, it is well known that surface waves may be brought into existence by introducing periodicity, in which case they are traditionally termed Rayleigh-Bloch

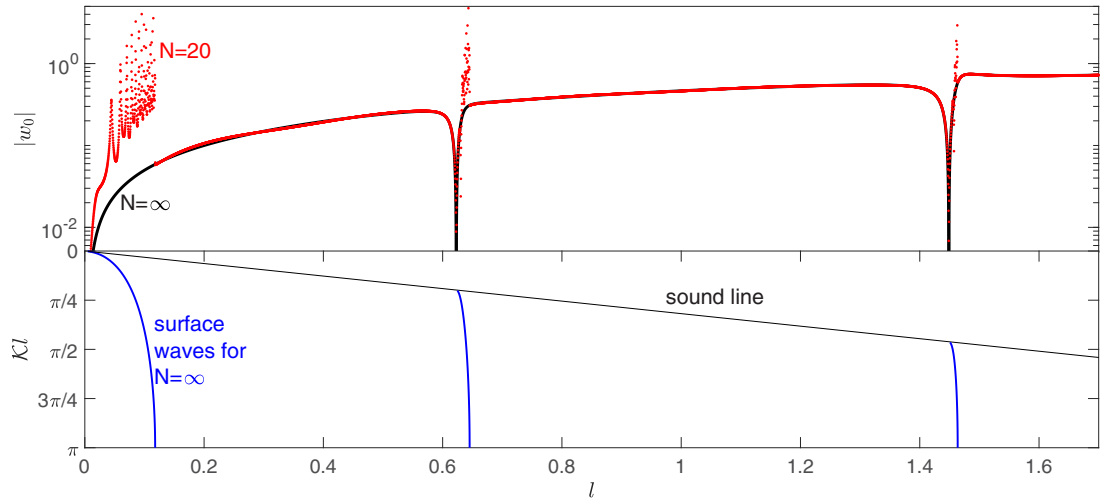

FIG. 10. (Top) Comparison between the near-field response for an infinite array and a finite array consisting of $2N + 1 = 41$ grooves. ($L/a = 10$ and $K = 1$ for both arrays.) (Bottom) Dispersion curves for surface waves guided by the infinite array; the sound line, representing propagation in the bulk, is also shown.

waves. Rayleigh-Bloch waves normally exist in frequency intervals where the wavelength in free space is comparable to the spacing; they resemble elastic Rayleigh waves while satisfying Bloch-periodicity conditions [63]. When the surface is decorated with a periodic array of subwavelength resonators, however, as in the present study, Rayleigh-Bloch may exist even when the spacing itself is subwavelength; such surface waves are termed "spoof plasmons," since they mimic electromagnetic surface-plasmon waves at a metal-dielectric interface [33–35,64].

To verify the existence of surface waves for the present configuration, we look for surface-wave solutions in the case of an infinite array. Accordingly, we disregard the incident (and reflected) plane wave and look for homogeneous solutions $Q(X, Y)$ that attenuate as $Y \to \infty$ and satisfy Bloch periodicity, namely, that

$$Q(X, Y)e^{-i\mathcal{K}X} \text{ is } l\text{-periodic in the coordinate } X, \tag{5.14}$$

where $\mathcal{K}$ is known as the Bloch wave number. As before, the grooves are treated as point-like isotropic scatterers characterized by the scattering coefficient A. This, together with condition (5.14), suggests the ansatz

$$Q \propto \sum_{n=-\infty}^{\infty} e^{inl\mathcal{K}} \mathcal{H}_0(R_n), \tag{5.15}$$

which is consistent with the Neumann condition on the solid substrate; since we are looking for surface-wave eigenfunctions, the constant of proportionality in (5.15) is immaterial. Application of Foldy's scheme to (5.15) yields the dispersion relation,

$$A\sigma(l, \mathcal{K}) = 1, \tag{5.16}$$

where A depends on l via (3.26) and (5.1), providing in turn an implicit relation between the spacing l (or frequency Ω) and the Bloch wave number $\mathcal{K}$.

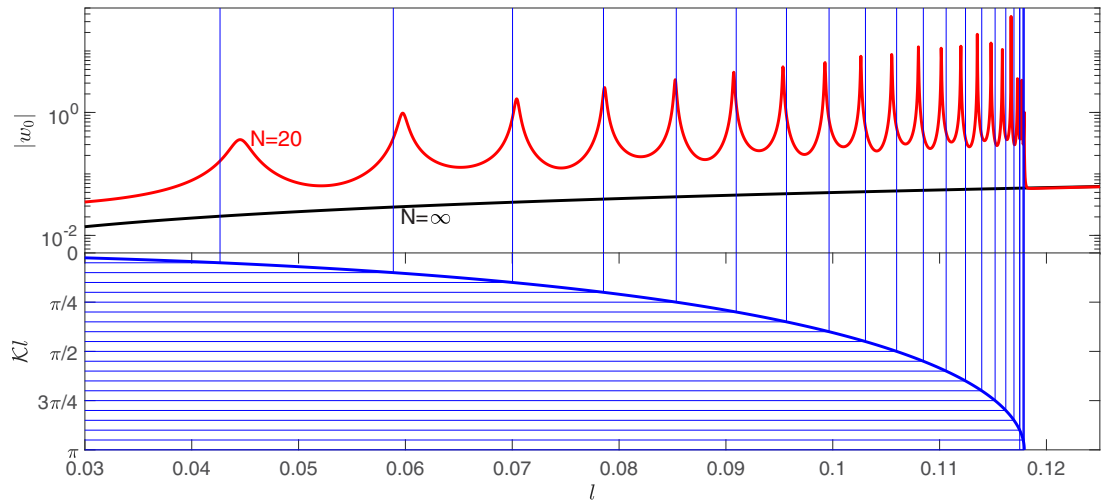

FIG. 11. Same as Fig. 10 but focused on a small-l interval. The added horizontal lines mark the $\mathcal{K}l$ values for which a whole number of surface-wave wavelengths fit the finite array: these are provided by (5.18) with $M = 1, 2, \ldots, 20$. The added vertical lines mark the corresponding l values, showing approximate agreement with the position of the resonant peaks of the finite array.

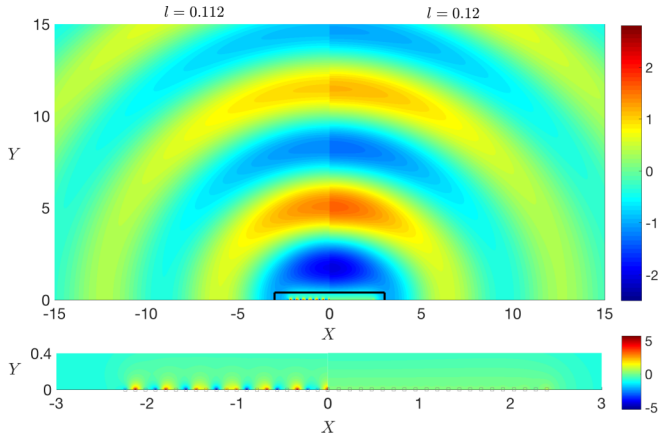

FIG. 12. Plane-wave scattering from a finite array of $2N+1=41$ grooves ($L/a=10$ and $K=1$). For $X<0$ ($X>0$), we plot Im Q for l just below (above) the cutoff of the first surface-wave branch (cf. Figs. 10 and 11). The inset zooms upon the array region.

Owing to time-reversal symmetry and the periodicity of the array, l is an even and 2π-periodic function of $\mathcal{K}l$. We may therefore restrict our attention to the irreducible Brillouin zone $0<\mathcal{K}l<\pi$ [65]. Moreover, since our interest is in surface-wave solutions that decay away from the array, we further limit our search to $l<\mathcal{K}l<\pi$, in which interval the bulk supports only evanescent waves [59]. Use of (3.26) and (5.7) to simplify (5.16) in that interval yields a real-valued dispersion relation:

$$\frac{1}{\pi}\ln\frac{l}{\pi\Omega\delta^{1/2}}+\frac{1}{\sqrt{\mathcal{K}^2l^2-l^2}}+\sum_{n\neq0}\left(\frac{1}{\sqrt{(\mathcal{K}l+2\pi n)^2-l^2}}-\frac{1}{2\pi|n|}\right)+\beta(K\chi^2\Omega^2)-\frac{1}{\chi^2\Omega^2V}=0. \tag{5.17}$$

We note that a similar dispersion relation has recently been derived for surface waves guided by an array of open-waveguide resonators [64].

To demonstrate the linkage between the anomalous response of a long-finite array and edge-excitation of surface waves, we solve (5.17) numerically for the same parameters as in Fig. 10; the resulting dispersion curves are shown in the lower part of that figure. We find several solution branches, whose l intervals of existence are precisely those where the long-finite array exhibits a highly oscillatory response. Furthermore, in Fig. 12, we plot the spatial distribution of the field Im Q for two values of l, just below and above the cutoff value of the first surface-wave branch, respectively; in the former case, the excitation of surface waves is clearly visible. We can also test our assertion that the multiple resonant peaks in the response of a finite array correspond to the formation of standing surface waves. Specifically, we test an heuristic approximation for the peak frequencies, to leading order in the limit $N\gg1$, obtained by requiring that a whole number M of surface wavelengths $2\pi/\mathcal{K}$ fits in the array; this gives

$$\mathcal{K}l\approx\frac{\pi M}{N}, \tag{5.18}$$

where we took $2Nl$ for the length of the array. Solving the dispersion relation (5.17), these values of $\mathcal{K}l$ transform into frequencies; in Fig. 11, we show that these frequencies predict the resonant peaks quite well. To improve on (5.18), we would need to carry out a detailed asymptotic analysis, which would undoubtedly uncover period-scale corrections to the assumed effective array length.

It is clear that there is a connection between frequency intervals which accommodate surface waves and the resonance frequencies of an isolated groove (compare Figs. 4 and 10). This connection can be studied via asymptotic analysis of the dispersion relation (5.17) close to the single-groove resonance frequencies [64], which are governed by (4.1). As an example, we obtain an approximation for the cutoff frequency of the first, deeply subwavelength, surface-wave branch (cf. Fig. 11). Thus, for $\mathcal{K}l=\pi$, approximating (5.17) to leading order in l, using (5.1) and (3.27), we find for the cutoff frequency

$$\Omega_c^2\sim\frac{\pi(3/K+2/V)}{\chi^2\ln(L/a)^2}, \tag{5.19}$$

with an $O(1/\ln^2(L/a))$ logarithmic error. Remarkably, (5.19) has the same form as the approximate expression (4.4) for the fundamental resonance of an isolated groove, except that the argument of the logarithm is $(L/a)^2$ instead of $1/\delta$.

E. Scattering from an acoustically compact array

We complete this section by considering the scattering from a finite array whose total length is small compared to the wavelength. We thereby wish to emphasize that such moderately long arrays scatter like a point scatterer, in contrast to an infinite array which scatters one or more plane waves [cf. (5.9)]. Specifically, we consider the diffracted field $Q^{(d)}=Q-2\cos Y$ [cf. (5.12)], or

$$Q^{(d)}=2\sum_{n=-N}^{N}w_n\mathcal{H}_0(R_n), \tag{5.20}$$

in the limit $l\ll1$ with N fixed. Using

$$R_n\sim R-nl\cos\phi+O(l^2)\quad\text{as}\quad l\to0, \tag{5.21}$$

where ϕ is a polar angle measured from the X axis (see Fig. 8), we find

$$Q^{(d)}\sim2\left(\sum_{n=-N}^{N}w_n\right)\mathcal{H}_0(R)+O(l^2)\quad\text{as}\quad l\to0, \tag{5.22}$$

where the $O(l)$ term vanishes because $\sum_{n=-N}^{N}nw_n=0$ by symmetry. Thus an acoustically compact array scatters isotropically. For the field distributions plotted in Fig. 12, $N=20$ and $l\approx0.1$, hence the total length of the array is ≈4, i.e., larger than half a wavelength; the deviations from isotropic scattering, observed specifically about $\phi=\pi/2$, are therefore unsurprising.

VI. CONCLUDING REMARKS

We have studied the acoustic response of an isolated cylindrical gas bubble, trapped in a micrometer-sized groove, to an incident plane wave. It exhibits multiple subwavelength extremities, namely, a fundamental Minnaert-like resonance followed by a sequence of higher-order resonance and antiresonance pairs. The fundamental resonance occurs in a low-frequency regime where the bubble dynamics are effectively characterized by a single degree of freedom, say the uniform gas pressure; the pinned meniscus retains an approximately parabolic profile with a curvature proportional to that pressure. At higher frequencies (still in the subwavelength regime), the meniscus is no longer parabolic and its dynamics become fully coupled with the compression and rarefaction of the gas and the spatial variations in the surrounding liquid pressure. Thus, in this regime, the meniscus profile is characterized by an infinite number of degrees of freedom (hence the infinite sequence of higher-order resonances). At the antiresonances, which closely precede the latter resonances, the liquid pressure and meniscus deformation appear to conspire to nullify the gas-pressure fluctuations (and hence the scattering), irrespective of the groove geometry, the gas properties and the local value of the incident pressure field. This robustness of the antiresonance frequencies may be useful for experimentally studying the meniscus dynamics as a function of a reduced set of parameters.

The acoustic response of a dilute array of trapped bubbles has also been studied. To this end, we have employed Foldy's point-scatterer approximation, with the frequency-response of an isolated bubble, as described above, entering via a complex-valued and frequency-dependent scattering coefficient. Although in this dilute limit the array spacing is assumed large compared to the groove size, interbubble interactions are strong and long range. In fact, pair interactions grow logarithmically with distance in the subwavelength regime, attenuating only on the scale of the wavelength. As a consequence, the resonances observed for an isolated bubble are shifted and diminished in amplitude in the problem of plane-wave scattering from an infinite dilute array; in fact, the first few resonant peaks disappear in the case where the array spacing is deeply subwavelength. (The antiresonances are robust to interference in the dilute limit.) The isolated-bubble resonances are manifested, however, in the phase response of the infinite array; in particular, near these resonances the phase of the reflected wave varies rapidly in between the values corresponding to acoustically rigid and soft homogeneous substrates. Furthermore, these resonances also give rise to surface-wave eigenstates of the infinite array, i.e., collective bubble oscillations propagating along the array and exponentially attenuating away from it. In particular, given the deeply subwavelength nature of the bubble resonances, arrays with subwavelength spacing support "spoof plasmon"-like surface waves, whose wavelength is small compared with the wavelength in the bulk. In those frequency intervals where surface waves exist, the acoustic response of a long-finite array markedly differs from that of an infinite array; this is due to edge-excitation of surface waves, which mediate interactions over arbitrary distances. In particular, these frequency intervals feature a set of resonant peaks which correspond to the formation of standing surface waves over the array.

We have carried out our investigation neglecting intrinsic (i.e., viscous and thermal) losses. This choice has been motivated by the hypothesis, corroborated by our analysis, that the resonances of a cylindrical bubble trapped in a micrometer-sized groove are damped (rather than weakly damped) radiatively; in particular, the gas- and liquid-pressure fluctuations in the vicinity of the bubble remain comparable in magnitude to the incident field. While in agreement with analyses of other two-dimensional scenarios [50–52], this finding sharply contrasts the more familiar three-dimensional scenarios of acoustically driven spherical bubbles and bubbles trapped in holes; in these cases radiation damping is weak and accordingly losses have a dramatic effect at resonance, even when the viscous and thermal boundary layers are narrow relative to the characteristic bubble size [43,45]. In the present two-dimensional scenario we anticipate that such narrow boundary layers have a perturbative effect, except perhaps in certain "singular" scenarios. In particular, at the high-order resonances and antiresonances, the radius of curvature of the meniscus may become locally comparable to the boundary-layer width. Also, losses will result in surface-wave attenuation, which, in turn, would substantially modify their dispersion at near-cutoff frequencies and dampen the standing-wave-type resonances predicted for long-finite arrays.

ACKNOWLEDGMENTS

O.S. is grateful for support from Engineering and Physical Sciences Research Council (EPSRC) through Grant No. EP/R041458/1. E.Y. was supported by the Israel Science Foundation (Grant No. 1081/16).

APPENDIX A: THERMODYNAMIC MODEL

In modeling bubble dynamics, it is a common practice to assume a thermodynamic-like description, where the gas pressure is assumed uniform—with its value being governed by the equation-of-state of an ideal gas. Generally speaking, that approach is incorrect due to the gas motion, see (2.7b). Nonetheless, our systematic approach leads, in the long-wavelength limit, to a uniform leading-order gas pressure. Since the Helmholtz equation is built upon the assumption of local isentropic processes, it is worthwhile to inspect whether the long-wavelength limit coincides with the results predicted by the "thermodynamic description."

For isentropic changes, the gas pressure satisfies an adiabatic-process equation, where the product of the (uniform) pressure $\bar{p}$ with the (two-dimensional) bubble volume, raised to the power κ, must equal $P(a^2V)^\kappa$. In the present linearized framework, where the meniscus deformation is small, the difference between the bubble volume and a^2V is proportional to $\int_{\mathcal{M}} \zeta \, ds$. The associated fractional change of the gas pressure is then given by

$$-\frac{\kappa}{a^2V}\int_{\mathcal{M}} \zeta \, ds. \tag{A1}$$

Condition (2.9) is accordingly replaced by

$$\gamma \frac{d^2\zeta}{ds^2} = p + \frac{\kappa P}{a^2V}\int_{\mathcal{M}} \zeta \, ds \quad \text{in} \quad M, \tag{A2}$$

while equations (2.5b) and (2.7b) and the velocity-continuity condition (2.11) are abandoned. Consistently, (2.17b) and (2.18b)–(2.19) are abandoned in the dimensionless formulation, as is (2.23), while (2.21a) is replaced by

$$\frac{d^2\eta}{dx^2} = q + \frac{K}{V}\int_{-1}^{1} \eta\, dx \quad \text{in} \quad M. \tag{A3}$$

Consider now the long-wavelength limit, where the gas pressure predicted by the "dynamic" description is rendered uniform, namely, (3.2), where $\mathcal{F}$ is defined by (3.3). Given (2.20) we find that condition (2.21a) coincides with condition (A3), which was derived using the "thermodynamic" description.

APPENDIX B: SOLUTIONS TO THE CANONICAL INNER PROBLEM

1. Elliptic-cylinder coordinates

We begin by introducing the elliptic-cylinder coordinates μ and ψ [66]. The constant-μ curves are the ellipses

$$\frac{x^2}{\cosh^2\mu} + \frac{y^2}{\sinh^2\mu} = 1, \tag{B1}$$

while the constant-ψ curves are the hyperboles

$$\frac{x^2}{\cos^2\psi} - \frac{y^2}{\sin^2\psi} = 1. \tag{B2}$$

In terms of these coordinates, the upper-half plane $y > 0$ is covered by the range $\mu > 0$ and $0 < \psi < \pi$, while $\mathcal{M}$ is the line $\mu = 0$. Note that at large r

$$\mu \sim \ln(2r) + o(1). \tag{B3}$$

Consider now the canonical problem (3.7)–(3.11) governing $\tilde{q}$. In terms of the elliptic-cylinder coordinates, condition (3.8) reads

$$\frac{\partial\tilde{q}}{\partial\psi} = 0 \quad \text{for} \quad \psi = 0, \pi. \tag{B4}$$

We accordingly seek a solution of Laplace's equation which satisfies both (B4) and (3.10) and is an even function of $\psi - \pi/2$. Using separation of variables in the elliptic-cylinder coordinates [66] and noting (B3) we readily obtain

$$\tilde{q} = \frac{1}{\pi}\mu + \sum_{m=0}^{\infty} A_m e^{-2m\mu}\cos 2m\psi. \tag{B5}$$

The coefficients $\{A_m\}_{m=0}^{\infty}$ are determined using condition (3.9), which apply at $\mu = 0$, together with the interface equations (3.12). Once these coefficients are determined, the value of β is provided as [cf. (3.15) and (B3)]

$$\beta = A_0. \tag{B6}$$

In what follows we first present an exact solution of the canonical problem governing $\tilde{q}$ and $\tilde{\eta}$. This is followed by the derivation of approximate solutions for small and large values of the parameter λ, defined in (3.13).

2. Exact solution

a. Dirichlet to Neumann mapping on $\mathcal{M}$

It is convenient to denote the pressure at $y = 0$ (with $|x| < 1$) as $\Pi(x)$,

$$\Pi(x) \stackrel{\text{def}}{=} \tilde{q}(x, y = 0) \quad \text{for} \quad |x| < 1, \tag{B7}$$

and temporarily regard it as given. The solution of (3.12) can then be readily obtained as

$$\tilde{\eta} = \int_{-1}^{1} G(x, x')\Pi(x')\, dx', \tag{B8}$$

wherein

$$G(x, x') = \frac{1}{2}\begin{cases}(x+1)(x'-1), & x < x'\\ (x'+1)(x-1), & x > x'\end{cases} \tag{B9}$$

is the Green function appropriate to (3.12).

Substituting (B8) into (3.9) provides $\partial\tilde{q}/\partial y$ at $\mathcal{M}$,

$$\frac{\partial\tilde{q}}{\partial y} = \lambda\int_{-1}^{1} G(x, x')\Pi(x')\, dx' \quad \text{for} \quad |x| < 1. \tag{B10}$$

From (3.11), we then find that

$$-\lambda\int_{-1}^{1}(1 - x'^2)\Pi(x')\, dx' = 2. \tag{B11}$$

b. Calculation of the Fourier coefficients

Differentiating (B5), we obtain

$$\left.\frac{\partial\tilde{q}}{\partial\mu}\right|_{\mu=0} = \frac{1}{\pi} - 2\sum_{m=1}^{\infty} mA_m\cos 2m\psi. \tag{B12}$$

Noting that

$$\left.\frac{\partial\tilde{q}}{\partial\mu}\right|_{\mu=0} = \sin\psi\left.\frac{\partial\tilde{q}}{\partial y}\right|_{y=0} \tag{B13}$$

we obtain, upon making use of the orthogonality of the trigonometric functions on $(0, \pi)$,

$$-mA_m = \frac{1}{\pi}\int_0^{\pi}\left.\frac{\partial\tilde{q}}{\partial y}\right|_{y=0}\cos 2m\psi\sin\psi\, d\psi, \quad m = 1, 2, \ldots \tag{B14}$$

In performing the integration we note that $x = \cos\psi$ at $\mu = 0$. This suggests employing the integration variable $\psi' \in (0, \pi)$, defined via $x' = \cos\psi'$, instead of x'. We therefore find that for $m \geqslant 1$

$$A_m + \frac{\lambda}{m\pi}\int_0^{\pi} d\psi\, \cos 2m\psi\sin\psi \times \int_0^{\pi} d\psi'\, G(x, x')\Pi(x')\sin\psi' = 0. \tag{B15}$$

It is readily verified that applying the above procedure for the zeroth mode simply reproduces (B11).

c. System of algebraic equations

With the function Π appearing in (B15), this equation set provides only a formal solution for $\{A_m\}_{m=1}^{\infty}$. Moreover, it does not provide A_0, which is expected to be determined by (B11). To close the problem, we substitute (B5) into (B7) to obtain

$$\Pi(x) = \sum_{n=0}^{\infty} A_n \cos 2n\psi. \tag{B16}$$

Substituting (B16) into (B11) gives

$$1 + 6\lambda \sum_{n=0}^{\infty} \frac{A_n}{16n^4 - 40n^2 + 9} = 0, \tag{B17}$$

which may be viewed as an equation governing A_0. Similarly, substituting (B16) into (B15) yields the infinite set of equations,

$$m\pi A_m + \lambda \sum_{n=0}^{\infty} \alpha_{mn} A_n = 0 \quad \text{for} \quad m \geqslant 1, \tag{B18}$$

wherein

$$\alpha_{mn} = \int_0^{\pi} d\psi \ \sin\psi \cos 2m\psi \int_0^{\pi} d\psi' \, G(x, x') \sin\psi' \cos 2n\psi' = 6(4m^2 - 1)^{-1}(4n^2 - 1)^{-1}$$
$$\times (4(m-n)^2 - 1)^{-1}(4(m-n)^2 - 9)^{-1}(4(m+n)^2 - 1)^{-1}(4(m+n)^2 - 9)^{-1}$$
$$\times (64m^6 - 16m^4(36n^2 + 11) + m^2(-576n^4 + 864n^2 + 76) + (1 - 4n^2)^2(4n^2 - 9)). \tag{B19}$$

For each $m \geqslant 1$, (B18) may be viewed as an equation governing A_m.

Equations (B17) and (B18) provide an infinite algebraic system governing the coefficients $\{A_m\}_{m=0}^{\infty}$. These equations are readily solved using controlled truncation. Once the coefficients are computed, we obtain β from (B6).

3. Strong surface tension (or low frequency)

In what follows, we supplement the above solutions with two asymptotic approximations. Consider first the limit $\lambda \ll 1$. Equations (3.9)–(3.11) suggest that $\tilde{\eta} = O(\lambda^{-1})$ while $\partial\tilde{q}/\partial y = O(1)$. This allows for a uniform $O(\lambda^{-1})$ term in $\tilde{q}$. We accordingly postulate the expansions

$$\tilde{q} = \lambda^{-1}\beta_{-1} + \tilde{q}_0(x, y) + \cdots, \quad \tilde{\eta} = \lambda^{-1}\tilde{\eta}_{-1}(x) + \cdots. \tag{B20a, b}$$

It follows from (3.12) that the surface displacement is approximately parabolic:

$$\tilde{\eta}_{-1} = \frac{x^2 - 1}{2}\beta_{-1}. \tag{B21}$$

Substitution into (3.9) and (3.11) gives

$$\beta_{-1} = -\tfrac{3}{2}. \tag{B22}$$

Combining (B20a) and (B22) furnishes approximation (3.27). Similarly, combining (B20b), (B21), and (B22) provides (3.28).

4. Weak surface tension

Consider now the limit $\lambda \to \infty$. In that limit, the kinematic condition (3.9) suggests that $\tilde{\eta}_0 \to 0$ for all $|x| < 1$, while the dynamic condition (3.12) implies that

$$\tilde{q} = o(1) \tag{B23}$$

on the meniscus $\mu = 0$. The corresponding limiting pressure field is then given by (B5) with $A_n = 0$ for all n, namely,

$$\tilde{q} = \frac{\mu}{\pi} + o(1). \tag{B24}$$

We thus find that

$$\beta = o(1). \tag{B25}$$

Inspecting the exact results for β we see that the above limit only holds sufficiently away from the singularities of β.

APPENDIX C: SINGULARITIES OF β

1. Eigenvalue problem for singularities of β

To determine the singularities of β we note that when $|\beta| \to \infty$ the $\ln r$ term in (3.15) is subdominant. The problem governing $\tilde{q}$ and $\tilde{\eta}$ is accordingly modified, with (3.10) being replaced by the condition of vanishing gradient at large distances. Since the remaining equations [namely, (3.7)–(3.9) and (3.12)] remain unaltered, the canonical problem becomes *homogeneous*. It admits nontrivial solutions only for certain values of λ, say $\{\lambda_a\}$. These solutions are determined up to a constant multiplier.

The eigenvalues $\{\lambda_a\}$ are readily determined using the solution scheme of Appendix B. Indeed, the above discussion implies that the solution of the canonical problem at antiresonance is of the form (B5) provided that the first term, proportional to μ, is omitted. The coefficients $\{A_n\}$ are then determined from (B17) without the forcing term,

$$\sum_{n=0}^{\infty} \frac{A_n}{16n^4 - 40n^2 + 9} = 0, \tag{C1}$$

and (B18). This combination constitutes a generalized eigenvalue problem for $1/\lambda_a$, which is readily solved; the first three values of λ_a are 75.11, 406.34, and 1179.41. For a given value of K, the corresponding antiresonance frequencies—say $\{\Omega_a\}$—are determined from (3.13).

2. Analysis close to singularities

Consider now the limit $\lambda \to \lambda_a$. Clearly for $0 < |\lambda - \lambda_a| \ll 1$ we have $\beta \gg 1$ and $\tilde{q} = O(\beta)$. How does β depends upon $\lambda - \lambda_a$?

We write the kinematic condition (3.9) as

$$\frac{\partial \tilde{q}}{\partial y} = \lambda_a \tilde{\eta} + (\lambda - \lambda_a)\tilde{\eta} \quad \text{for} \quad \mu = 0. \tag{C2}$$

When $\lambda = \lambda_a$ we know that the first two terms balance. The last term is related to $O(1)$ flux, see (3.11). It follows that $\tilde{\eta}$, and whence also $\tilde{\beta}$, scale as $(\lambda - \lambda_a)^{-1}$. We accordingly postulate the expansions

$$\tilde{q} \sim \frac{1}{\lambda - \lambda_a}\tilde{q}_{-1} + \tilde{q}_0 + \cdots, \quad \tilde{\eta} \sim \frac{1}{\lambda - \lambda_a}\tilde{\eta}_{-1} + \tilde{\eta}_0 + \cdots, \tag{C3}$$

and similarly expand

$$\beta \sim \frac{1}{\lambda - \lambda_a}\beta_{-1} + \beta_0 + \cdots. \tag{C4}$$

The leading-order pressure $\tilde{q}_{-1}$ is governed by Laplace's equation. At $y = 0$ it satisfies a homogeneous Neumann condition for $|x| > 1$ [see (3.8)] and the kinematic condition [cf. (3.9)]

$$\frac{\partial \tilde{q}_{-1}}{\partial y} = \lambda_a \tilde{\eta}_{-1} \tag{C5}$$

for $|x| < 1$. At large r, it satisfies [cf. (3.15)]

$$\tilde{q}_{-1} \to \beta_{-1} \quad \text{as} \quad r \to \infty. \tag{C6}$$

The corresponding leading-order displacement satisfies [cf. (3.12)]

$$\frac{d^2\tilde{\eta}_{-1}}{dx^2} = \tilde{q}_{-1} \quad \text{for} \quad |x| < 1, \qquad \tilde{\eta}_{-1} = 0 \quad \text{at} \quad x = \pm 1. \tag{C7a, b}$$

This is the homogeneous problem which has been described earlier. It is solvable for the singular values λ_a. Note that the multiplicative freedom leaves β_{-1} undetermined.

To determine β_{-1}, we consider the next asymptotic order. The $O(1)$ fields $\tilde{q}_0$ and $\tilde{\eta}_0$ satisfy a forced version of the leading-order problem, whose solvability condition yields β_{-1}. Indeed, the problem governing $\tilde{q}_0$ and $\tilde{\eta}_0$ is the same as that outlined above for $\tilde{q}_{-1}$ and $\tilde{\eta}_{-1}$, except that the kinematic condition (C2) now gives

$$\frac{\partial \tilde{q}_0}{\partial y} = \lambda_a \tilde{\eta}_0 + \tilde{\eta}_{-1} \tag{C8}$$

instead of (C5), while the far-field condition is

$$\tilde{q}_0 \sim \frac{1}{\pi} \ln r + O(1). \tag{C9}$$

Making use of the second Green identity in conjunction with Laplace's equation governing $\tilde{q}_{-1}$ and $\tilde{q}_0$ yields

$$\oint \left(\tilde{q}_0 \frac{\partial \tilde{q}_{-1}}{\partial n} - \tilde{q}_{-1} \frac{\partial \tilde{q}_0}{\partial n} \right) dl = 0, \tag{C10}$$

where the integration is carried out over a closed contour on which dl is a differential length element and $\partial/\partial n$ denotes differentiation in the outward-normal direction. In what follow, we choose the contour as the union of a line segment on the x axis, extending from $x = -R$ to $x = R$, and a semicircular arc of radius R, centered about the origin, in the liquid domain. Making use of the far-field conditions (C6) and (C9) together with the mixed conditions which govern $\tilde{q}_{-1}$ and $\tilde{q}_0$ at $y = 0$ we obtain

$$\beta_{-1} = \int_{-1}^{1} \frac{d^2\tilde{\eta}_{-1}}{dx^2}\tilde{\eta}_{-1}\, dx + \lambda_a \times \int_{-1}^{1} \left(\tilde{\eta}_0 \frac{d^2\tilde{\eta}_{-1}}{dx^2} - \frac{d^2\tilde{\eta}_0}{dx^2}\tilde{\eta}_{-1} \right) dx, \tag{C11}$$

where the left-hand side is contributed from the semicircular arc. Integration by parts in conjunction with the pinning conditions reveals that the second integral on the right-hand side vanishes; integration by parts of the first integral on the right-hand side then yields

$$\beta_{-1} = -\int_{-1}^{1} \left(\frac{d\tilde{\eta}_{-1}}{dx} \right)^2 dx. \tag{C12}$$

Combining with (C4) thus furnishes (3.29).

[1] J. B. Pendry, Phys. Rev. Lett. **85**, 3966 (2000).
[2] D. R. Smith, J. B. Pendry, and M. C. K. Wiltshire, Science **305**, 788 (2004).
[3] J. B. Pendry, D. Schurig, and D. R. Smith, Science **312**, 1780 (2006).
[4] S. A. Maier, *Plasmonics: Fundamentals and Applications* (Springer Science & Business Media, 2007).
[5] S. A. Cummer, J. Christensen, and A. Alù, Nat. Rev. Mater. **1**, 16001 (2016).
[6] G. W. Stewart and R. B. Lindsay, *Acoustics: A Text on Theory and Applications* (Chapman and Hall, New York, 1931).
[7] F. Fahy, *Sound and Structural Vibration* (Academic Press, Oxford, 1987).
[8] Z. Yang, J. Mei, M. Yang, N. H. Chan, and P. Sheng, Phys. Rev. Lett. **101**, 204301 (2008).
[9] M. Yang, G. Ma, Z. Yang, and P. Sheng, Phys. Rev. Lett. **110**, 134301 (2013).
[10] T. Leighton, *The Acoustic Bubble* (Academic Press, London, 2012).
[11] B. B. Goldberg, J.-B. Liu, and F. Forsberg, Ultrasound Med. Biol. **20**, 319 (1994).
[12] B. Dollet, P. Marmottant, and V. Garbin, Annu. Rev. Fluid Mech. **51** (2019).
[13] A. A. Ruffa, J. Acoust. Soc. Am. **91**, 1 (1992).
[14] M. Kafesaki, R. S. Penciu, and E. N. Economou, Phys. Rev. Lett. **84**, 6050 (2000).
[15] C. Goffaux and J. P. Vigneron, Physica B: Condens. Matter **296**, 195 (2001).
[16] R. Sainidou, N. Stefanou, and A. Modinos, Phys. Rev. B **74**, 172302 (2006).

[17] A. Bretagne, A. Tourin, and V. Leroy, Appl. Phys. Lett. **99**, 221906 (2011).

[18] V. Leroy, A. Strybulevych, M. Lanoy, F. Lemoult, A. Tourin, and J. H. Page, Phys. Rev. B **91**, 020301(R) (2015).

[19] M. Lanoy, R. Pierrat, F. Lemoult, M. Fink, V. Leroy, and A. Tourin, Phys. Rev. B **91**, 224202(R) (2015).

[20] M. Lanoy, R.-M. Guillermic, A. Strybulevych, and J. H. Page, Appl. Phys. Lett. **113**, 171907 (2018).

[21] M. Minnaert, Philos. Mag. **16**, 235 (1933).

[22] D. G. Crighton, A. P. Dowling, J. E. F. Williams, M. A. Heckl, and F. A. Leppington, *Modern Methods in Analytical Acoustics: Lecture Notes* (Springer Science & Business Media, New York, 2012).

[23] V. Leroy, A. Bretagne, M. Fink, H. Willaime, P. Tabeling, and A. Tourin, Appl. Phys. Lett. **95**, 171904 (2009).

[24] E. L. Thomas, Nature (London) **462**, 990 (2009).

[25] D. C. Calvo, A. L. Thangawng, C. N. Layman, Jr., R. Casalini, and S. F. Othman, J. Acoust. Soc. Am. **138**, 2537 (2015).

[26] V. Leroy, A. Bretagne, M. Lanoy, and A. Tourin, AIP Adv. **6**, 121604 (2016).

[27] A. A. Doinikov and A. Bouakaz, IEEE Trans. Ultrason. Ferroelectr. Freq. Control **58**, 981 (2011).

[28] T. Faez, M. Emmer, K. Kooiman, M. Versluis, A. F. W. van der Steen, and N. de Jong, IEEE Trans. Ultrason. Ferroelectr. Freq. Control **60**, 7 (2013).

[29] H. Ammari, B. Fitzpatrick, H. Lee, E. O. Hiltunen, and S. Yu, arXiv:1810.12756 [J. Differ. Eqs. (to be published)].

[30] B. Bhushan and Y. C. Jung, Prog. Mater. Sci. **56**, 1 (2011).

[31] D. Quéré, Annu. Rev. Mater. Res. **38**, 71 (2008).

[32] J. P. Rothstein, Annu. Rev. Fluid Mech. **42**, 89 (2010).

[33] J. B. Pendry, L. Martin-Moreno, and F. J. Garcia-Vidal, Science **305**, 847 (2004).

[34] F. J. Garcia-Vidal, L. Martin-Moreno, and J. B. Pendry, J. Opt. A: Pure Appl. Opt. **7**, S97 (2005).

[35] L. Quan, F. Qian, X. Liu, X. Gong, and P. A. Johnson, Phys. Rev. B **92**, 104105 (2015).

[36] H. Ammari and H. Zhang, SIAM J. Appl. Math. **49**, 3252 (2017).

[37] H. Ammari, B. Fitzpatrick, D. Gontier, H. Lee, and H. Zhang, SIAM J. Appl. Math. **77**, 1827 (2017).

[38] H. Ammari, B. Fitzpatrick, D. Gontier, H. Lee, and H. Zhang, Proc. R. Soc. A **473**, 20170469 (2017).

[39] H. Ammari, B. Fitzpatrick, H. Lee, S. Yu, and H. Zhang, arXiv:1709.08177.

[40] H. Ammari, B. Fitzpatrick, H. Lee, E. O. Hiltunen, and S. Yu, arXiv:1811.03905.

[41] D. L. Miller and W. L. Nyborg, J. Acoust. Soc. Am. **73**, 1537 (1983).

[42] D. L. Miller, J. Acoust. Soc. Am. **104**, 2498 (1998).

[43] H. Rathgen, K. Sugiyama, C.-D. Ohl, D. Lohse, and F. Mugele, Phys. Rev. Lett. **99**, 214501 (2007).

[44] K. Sugiyama and H. Rathgen, Theor. Appl. Mech. Jpn. **58**, 251 (2010).

[45] H. Gelderblom, A. G. Zijlstra, L. van Wijngaarden, and A. Prosperetti, Phys. Fluids **24**, 122101 (2012).

[46] A. Zijlstra, D. F. Rivas, H. J. G. E. Gardeniers, M. Versluis, and D. Lohse, Ultrasonics **56**, 512 (2015).

[47] R. Bolaños-Jiménez, M. Rossi, D. F. Rivas, C. J. Kähler, and A. Marin, J. Fluid. Mech. **820**, 529 (2017).

[48] D. Gritsenko, Y. Lin, V. Hovorka, Z. Zhang, A. Ahmadianyazdi, and J. Xu, Phys. Fluids **30**, 082001 (2018).

[49] A. Prosperetti, Ultrasonics **22**, 69 (1984).

[50] D. Epstein and J. B. Keller, J. Acoust. Soc. Am. **52**, 975 (1972).

[51] Y. A. Ilinskii, T. A. Hay, E. A. Zabolotskaya, and M. F. Hamilton, J. Acoust. Soc. Am. **130**, 2370 (2011).

[52] Y. A. Ilinskii, E. A. Zabolotskaya, T. A. Hay, and M. F. Hamilton, J. Acoust. Soc. Am. **132**, 1346 (2012).

[53] C. J. Teo and B. C. Khoo, Microfluid. Nanofluidics **7**, 353 (2009).

[54] A. M. J. Davis and E. Lauga, Phys. Fluids **21**, 011701 (2009).

[55] E. J. Hinch, *Perturbation Methods* (Cambridge University Press, Cambridge, 1991).

[56] E. L. Carstensen and L. L. Foldy, J. Acoust. Soc. Am. **19**, 481 (1947).

[57] P. A. Martin, *Multiple Scattering: Interaction of Time-Harmonic Waves with N Obstacles*, (Cambridge University Press, Cambridge, 2006).

[58] D. G. Crighton and F. G. Leppington, Proc. R. Soc. Lond. A **335**, 313 (1973).

[59] C. M. Linton, J. Eng. Math. **33**, 377 (1998).

[60] M. Born and E. Wolf, *Principles of Optics: Electromagnetic Theory of Propagation, Interference and Diffraction of Lght* (Elsevier, 2013).

[61] H. D. Maniar and J. N. Newman, J. Fluid Mech. **339**, 309 (1997).

[62] I. Thompson, C. M. Linton, and R. Porter, Quart. J. Mech. Appl. Math. **61**, 333 (2008).

[63] D. V. Evans and C. M. Linton, Quart. J. Mech. Appl. Math. **46**, 643 (1993).

[64] O. Schnitzer, Phys. Rev. B **96**, 085424 (2017).

[65] L. Brillouin, *Wave Propagation in Periodic Structures: Electric Filters and Crystal Lattices* (Dover, 1953).

[66] P. Moon and D. E. Spencer, *Field Theory Handbook* (Springer-Verlag, New York, 1988).